Politecnico di Milano

Scuola di Ingegneria Industriale e dell'Informazione

Corso di Laurea Magistrale in Ingegneria Fisica

Dipartimento di Fisica

Magnetic Resonant Inelastic X-Ray Scattering of Layered Perovskite Iridates at High Pressure and Optical Schemes for Improving the Energy Resolution

Relatore:

Prof. Giacomo GHIRINGHELLI

Correlatori:

Dott. Marco MORETTI
Dott. Michael KRISCH

Tesi di Laurea di:

Margherita REZZAGHI
Matr. 804334

Anno Accademico 2014-2015

"Never stop fighting till the fight is done."
Eliot Ness, *The Untouchables*

Abstract

This thesis work concerns a magnetic high pressure RIXS study of the $Sr_3Ir_2O_7$ compound. The measurements were performed at beam line ID20 of the European Synchrotron Radiation Facility, Grenoble.

The motivation behind this work is that $5d$ transition metal oxides have recently attracted attention due to their peculiar properties, such as their unexpected insulating behaviour. In fact the Hubbard model, which gives a successful explanation of the electronic structure of $3d$ metal oxides, can not be naively invoked to explain the ground state properties of these compounds, including the one of our interest, $Sr_3Ir_2O_7$, the second member of the Ruddlesden-Popper series $(Sr_{n+1}Ir_nO_{3n+1})$. The opening of the gap responsible for the insulating behaviour is due to the strong spin orbit coupling which forms the so-called $J_{\text{eff}} = 1/2$ state. However, even if a model for the ground state has now been developed, the magnetic behaviour of this material is still not well understood so far. Indeed at least two theories were elaborated to interpret the magnetic excitation spectrum of $Sr_3Ir_2O_7$, but none of those satisfactorily accounts for all the experimental observations.

In this thesis we intend to utilise the Ir L_3 edge resonant inelastic X-ray scattering (RIXS) technique and, by applying pressure, we intend to study the response of magnetic excitations to external stimuli. This is necessary to provide new experimental evidences which pose further constraints on the theoretical models. However, those presented here are the first measurements of magnetic excitations performed with RIXS under high pressure, and unfortunately the acquired data are not sufficient to confirm any of the existing theoretical models. Anyway our study paves the way for future experiments at higher pressures, essential to develop a complete theory for magnetic excitations in iridates.

This thesis also comprises a part devoted to the development of new instru-

mentation which allows us to improve the experimental energy resolution. The main motivation is three-fold: i) a better energy resolution would allow the separation of closely lying magnon branches or other types of excitations, which would otherwise be indistinguishable; ii) lattice vibrations, i.e. phonons, could then become accessible to RIXS. These are hardly accessible with the current set-up, but are extremely interesting as one could extract quantitative information on the electron-phonon coupling; iii) the width of magnetic excitations is nowadays energy resolution limited and a precise assessment of their intrinsic life time is precluded. Assessing the line width of excitations beyond the experimental energy resolution would shed light on possible decay mechanisms and couplings to other quasi-particles. Our calculations and simulations show that an experimental energy resolution as good as 5 meV can be achieved.

Sommario

Gli ossidi dei metalli di transizione $3d$ sono tra i materiali che hanno suscitato maggiore interesse negli ultimi decenni, soprattutto per alcune loro caratteristiche, come per esempio le transizioni metallo-isolante in alcuni sistemi a forte correlazione elettronica. Molti di questi composti sono descritti con successo dal modello di Hubbard, che fornisce una spiegazione riguardo le loro proprietà di trasporto. In particolare questa teoria si basa su due diversi concetti: la sovrapposizione tra orbitali (che favorisce un comportamento metallico) e la repulsione tra due elettroni che occupano lo stesso sito (che favorisce un comportamento isolante). Tuttavia negli ultimi anni l'attenzione dei ricercatori è stata attratta anche dagli ossidi di metalli di transizione $4d$ e $5d$, a causa di alcune loro inaspettate proprietà. Infatti la più larga estensione spaziale degli orbitali rispetto a quella dei $3d$ dovrebbe favorire un comportamento metallico, mentre alcuni di questi materiali, come i primi due membri della serie di Ruddlesden-Popper $Sr_{n+1}Ir_nO_{3n+1}$ (Sr_2IrO_4 e $Sr_3Ir_2O_7$), possiedono caratteristiche isolanti. Una spiegazione di questa proprietà è stata fornita dalla cosiddetta teoria del $J_{eff} = 1/2$, in cui si tiene conto dell'accoppiamento spin-orbita nella modellizzazione della struttura elettronica. Questo, infatti, insieme al campo cubico dovuto alla simmetria del cristallo e alla repulsione elettrone-elettrone, è in grado di aprire una gap e indurre un comportamento isolante.

Tuttavia, sebbene sia presente una teoria in larga parte accettata per spiegare le proprietà isolanti di questi composti, non si può dire altrettanto riguardo il loro comportamento magnetico. In particolare la descrizione delle eccitazioni magnetiche è risultata finora ambigua e non è ancora del tutto chiara. Recenti misure mostrano che il composto $Sr_3Ir_2O_7$, oggetto di questo studio, presenta due eccitazioni magnetiche quasi degeneri con una gap relativamente grande di circa 90 meV. Le osservazioni sperimentali sono state spiegate

utilizzando due modelli che sono fondamentalmente diversi, evidenziando la mancanza di una profonda comprensione dei fenomeni osservati.

Questa tesi ha lo scopo di fare chiarezza e fornire nuove evidenze sperimentali per aiutare a comprendere il comportamento magnetico di $Sr_3Ir_2O_7$. Il nostro esperimento consiste nell'effettuare misure delle eccitazioni magnetiche ad alte pressioni con la tecnica della diffusione risonante anelastica di radiazione X dura (RIXS) alla soglia L_3 dell'iridio. Infatti, con l'aiuto di uno stimolo esterno, in questo caso la pressione, potrebbe essere possibile fornire nuovi dati sperimentali e confermare o smentire le precedenti teorie. Per effettuare queste misure è stato necessario implementare un complicato set-up sperimentale. Il campione è stato inserito all'interno di una Diamond Anvil Cell, che permette, attraverso l'utilizzo di due diamanti, di applicare la pressione desiderata. In questo caso è però necessario inserire il materiale studiato anche al centro di un anello di berillio, affinchè il gas iniettato per assicurare una distribuzione anisotropa della pressione rimanga confinato nella camera del campione. Questo, però, genera alcuni inconvenienti: in particolare, uno dei maggiori problemi consiste nella diffusione elastica e anelastica del berillio, il cui contributo può mascherare del tutto il segnale proveniente dal campione. Per ovviare a questo problema abbiamo sviluppato un sistema di fenditure motorizzate per mascherare il segnale spurio. Un'ulteriore complicazione deriva dal fatto che l'esperimento deve essere effettuato a temperature inferiori alla temperatura di Nèel del sistema ($T_N \sim$ 230 K). Per questo, la cella di diamanti contenente il campione e le fenditure motorizzate sono installate all'interno di un criostato ad azoto, limitando enormemente i gradi di libertà del set-up sperimentale. Quelle presentate in questa tesi sono le prime misure di eccitazioni magnetiche ottenute mediante RIXS ad alte pressioni. Sebbene il set di dati raccolto non sia completo per poter discriminare fra le due teorie avanzate in letteratura, abbiamo dimostrato la fattibilità di questo tipo di esperimenti aprendo la strada ad esperimenti futuri in questo campo.

Questa tesi comprende inoltre una parte riguardante un nuovo set-up sperimentale che ha il fine di migliorare la risoluzione in energia. Le principali motivazioni sono tre: i) una migliore risoluzione permetterebbe di distinguere modi magnetici e altre eccitazioni che si trovano ad energie prossime e che altrimenti risulterebbero indistinguibili; ii) sarebbe possibile studiare le vibrazioni del reticolo, i.e. i fononi, inaccessibili con l'odierno set-up, che po-

trebbero dare informazioni quantitative riguardo l'accoppiamento elettrone-fonone; iii) la larghezza di banda delle eccitazioni è limitata dalla risoluzione in energia e non risulta quindi possibile assegnare un valore preciso al loro tempo di vita. Con una migliore risoluzione sarebbe possibile ottenere informazioni riguardo possibili meccanismi di decadimento e accoppiamento con altre quasi-particelle.

Questo nuovo set-up è formato da un monocromatore e da uno spettrometro. Il primo è basato sul concetto CDW proposto da Y. Shvyd'ko: un primo elemento C collima la radiazione (nel caso della beam line ID20 è già presente il primo elemento ottico che svolge questa funzione e pertanto risulta inutile aggiungerlo); un secondo elemento D disperde la radiazione: grazie a un cristallo tagliato asimmetricamente si crea infatti nel fascio riflesso un legame tra energia e angolo di riflessione e quindi un ventaglio di lunghezze d'onda (per questo il monocromatore è chiamato anche "rainbow"); infine un terzo elemento W, grazie a un cristallo simmetrico, seleziona una sola lunghezza d'onda. In questo modo si ottiene una risoluzione in energia pari a ~ 3 meV. Per quanto riguarda lo spettrometro, esso potrebbe essere basato sullo stesso principio CDW del monocromatore (aggiungendo un sistema ottico subito prima del cristallo asimmetrico per collimare il fascio diffuso), ma semplici considerazioni evidenziano che la divergenza residua del fascio diffuso dal campione comprometterebbe parzialmente la risoluzione in energia dello spettrometro. Per questo motivo in questa tesi è inoltre suggerita un'altra implementazione per quest'ultimo: si potrebbe infatti sostituire gli analizzatori di Si(844) utilizzati tuttora presso ID20 con altri di α-SiO$_2$(039). Questo, grazie alla minore risoluzione intrinseca in energia di questo materiale, permetterebbe di raggiungere una risoluzione di ~ 5 meV. Tuttavia, l'impiego di quarzo per la fabbricazione di analizzatori potrebbe richiedere uno sforzo considerevole per sviluppare un processo di produzione che attualmente é ottimizzato esclusivamente per gli analizzatori di Si.

Contents

List of Figures

List of Tables

Chapter 1

Introduction

1.1 Introduction to RIXS

Recently resonant inelastic X-ray scattering (RIXS) has been routinely used to investigate the electronic structure of various materials. The development of this technique has been made possible by the availability of third-generation synchrotron radiation sources, partially overcoming the limitations imposed by the low cross-section of the RIXS process. RIXS is a *photon-in photon-out* spectroscopic technique. An incident photon of energy $\hbar\omega_1$ and momentum $\hbar\mathbf{k}_1$ is scattered by the studied system and changes its energy and momentum, as shown in Figure 1.1. By analysing the energy of the scattered photon at a specific scattering angle (2θ), one can determine the energy E $= \hbar\omega_1$ - $\hbar\omega_2$ and momentum transfer $\hbar\mathbf{q} = \hbar\mathbf{k}_1$ - $\hbar\mathbf{k}_2$ transferred to the sample. Also, an additional parameter that can be tuned is the incident photon polarisation and in a few cases polarisation analysis of the scattered photons can be performed.

In RIXS the incident photon energy $\hbar\omega_1$ is tuned to an absorption edge of one of the atomic species in the sample. This gives rise to the resonant promotion of an electron from a core shell to the empty valence band, as shown in Figure 1.2. After the absorption the system is in an excited state for a time span, given by the core-hole life-time. In the decay process, en electron falls again in the core level, causing the emission of an other photon. The final state can either be the ground state itself or an excited state of higher energy. In the former case, elastic scattering occurs, whereas in the latter the process is said to be inelastic, since a fraction of the incident photon energy
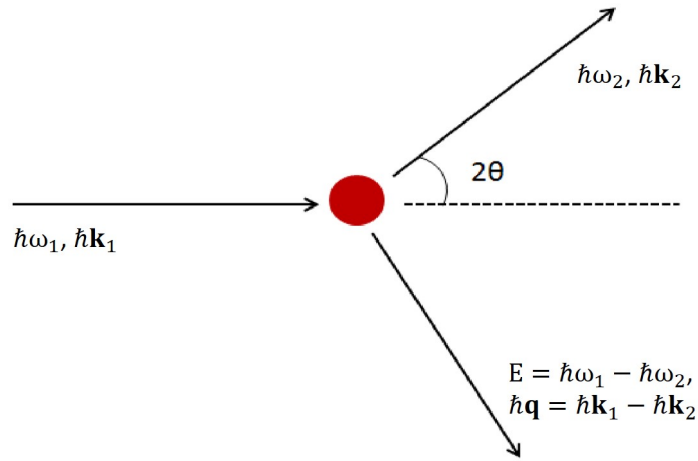
Figure 1.1: Inelastic scattering process: the incoming photon with momentum $\hbar\mathbf{k}_1$ and energy $\hbar\omega_1$ is scattered at an angle of 2θ into a photon with energy $\hbar\omega_2$ and momentum $\hbar\mathbf{k}_2$.
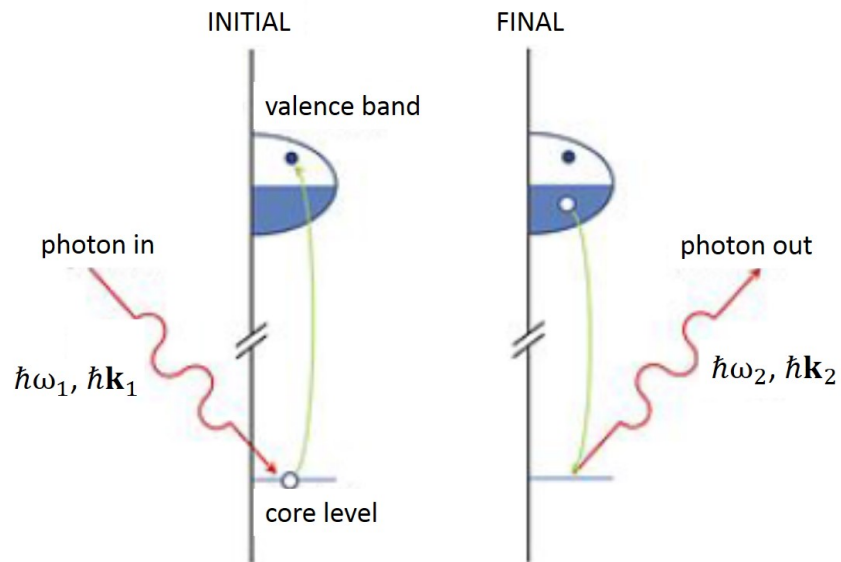
Figure 1.2: RIXS process: a core level electron is promoted to a valence band state and then decays emitting the scattered photon[1].
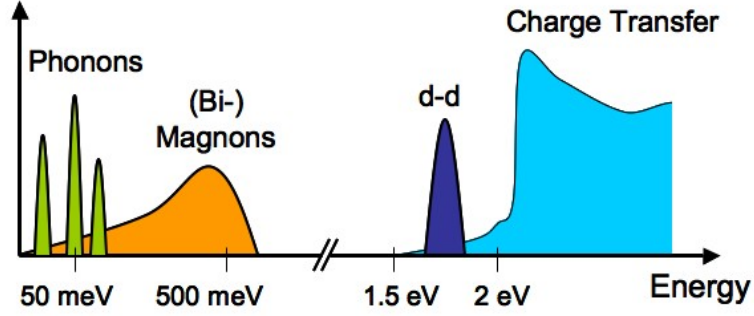
Figure 1.3: RIXS excitations: as the energy difference E $= \hbar\omega_1 - \hbar\omega_2$ increases, the present features are phonons, magnons and bimagnons, $d-d$ and charge transfer excitations[1].

has been transferred to the system. For these reasons RIXS is a good technique to study fundamental excitations in materials. The key to understand the system is the excitation spectrum as depicted in Figure 1.3. It is usually shown as a function of energy transfer in order to highlight the energy of the various excitations that can be studied: at zero energy transfer is the elastic line, while at increasing energy losses one typically finds phonons, single and higher order magnons, crystal field and charge transfer excitations, etc... RIXS offers advantages compared to other scattering techniques:

- enhancement of the scattering cross-section due to the resonant term;

- site and orbital sensitivity[1].

To better understand the RIXS theory it is necessary to delineate the proper Hamiltonian and cross-section. In particular the fundamental term is given by the Kramers-Heisenberg formula, which represents the double differential scattering cross-section in RIXS process. This can be derived as follow. The system Hamiltonian can be written as:

$$\hat{H} = \hat{H}_0 + \hat{H}_i. \tag{1.1}$$

Here $\hat{H}_0$ represents the non-interactive term given by the sum of the kinetic and potential energy of the electrons in the crystal as in the following:

$$\hat{H}_0 = \sum_j \left[\frac{\mathbf{p}_j^2}{2m} + \mathbf{V}(\mathbf{r}_j) \right] \tag{1.2}$$

where $\mathbf{p}_j$ and $\mathbf{r}_j$ are respectively the momentum and the position operator for the j electron and m its mass. $\hat{H}_i$, instead, is the interaction term between the radiation field and the sample electrons, given by

$$\hat{H}_i = \sum_j \left[\frac{e}{mc} \mathbf{p}_j \cdot \mathbf{A}(\mathbf{r}_j) + \frac{e^2}{2mc^2} \mathbf{A}^2(\mathbf{r}_j) \right] \tag{1.3}$$

where $\mathbf{A}(\mathbf{r}_j)$ is the potential vector operator referred to the electromagnetic wave at the position $\mathbf{r}_j$ of the electron j, e the electron charge, and c the velocity of light in vacuum.

The transition rate of an electronic excitation from an initial state to a final one is given by the Fermi golden rule applied to the interaction term of the Hamiltonian $\hat{H}_i$:

$$w_{i \rightarrow f} = \frac{1}{\hbar} \left| \langle f | \hat{H}_i | i \rangle + \sum_n \frac{\langle f | \hat{H}_i | n \rangle \langle n | \hat{H}_i | i \rangle}{E_n - E_i} \right|^2 \delta(E_f - E_i - \hbar\omega) \tag{1.4}$$

where $|i\rangle$, $|n\rangle$ and $|f\rangle$ are respectively the initial, intermediate and final states and E_i, E_n and E_f their energies. Considering that in RIXS the process takes place in resonant conditions, the second term in Equation 1.4 is dominant. The Kramers-Heisenberg double differential cross-section can thus be derived considering only terms linear in $\mathbf{A}(\mathbf{r}_j)$ and rewritten as:

$$\frac{\mathrm{d}^2\sigma}{\mathrm{d}\Omega \mathrm{d}\hbar\omega_2} = r_0^2 (\frac{\omega_2}{\omega_1}) \sum_f \left| (\frac{\hbar}{m}) \sum_n \frac{\langle f | (\boldsymbol{\epsilon}_2^* \cdot \mathbf{p}_j) e^{-i\mathbf{k}_2 \cdot \mathbf{r}_j} | n \rangle \langle n | (\boldsymbol{\epsilon}_1 \cdot \mathbf{p}_j) e^{i\mathbf{k}_1 \cdot \mathbf{r}_j'} | i \rangle}{E_i - E_n + \hbar\omega_1 - i\Gamma_n/2} \right|^2$$
$$\times \delta(E_i - E_f + \hbar\omega). \tag{1.5}$$

Here $\boldsymbol{\epsilon}_1$ and $\boldsymbol{\epsilon}_2$ are the polarisations of the incident and scattered photon respectively and Γ_n is the energy broadening of the intermediate state.

This represents the probability that a photon is scattered from an initial state $|i\rangle$ to a final state $|f\rangle$ in a solid angle $\mathrm{d}\Omega$ with energy $\mathrm{d}\hbar\omega_2$[2, 3].

1.2 Magnetic RIXS

In the last years, improvements in the instrumental energy resolution and in the theoretical understanding of the RIXS process made scientists realise
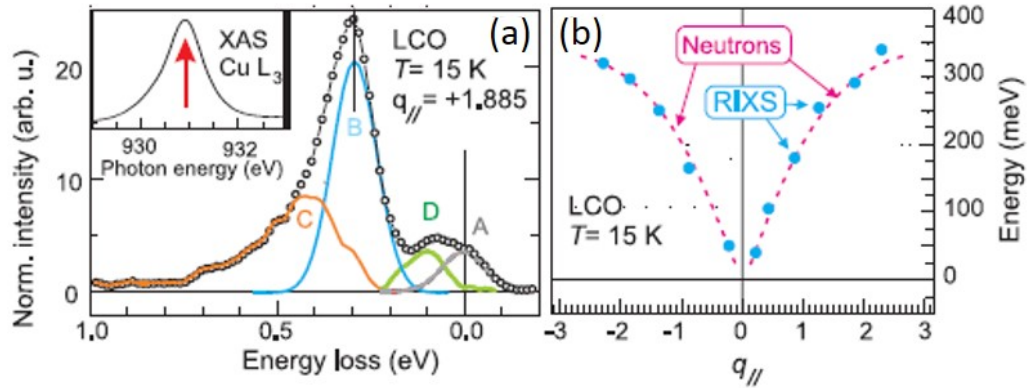
Figure 1.4: (a) RIXS spectrum of La_2CuO_4 with relative spectral features: elastic (A) and single magnon (B) peaks, multiple magnon (C) and optical phonons (D). (b) single magnon dispersion measured by RIXS (blue dots) compared to the one measured by neutron scattering (dashed purple line)[5].

that single magnons could be studied with this technique. This is rather counter-intuitive, as RIXS is usually satisfactorily described by two consecutive electric dipole, i.e. spin-conserving/transitions. However, when performed at a spin-orbit split edge (like the Cu or Ir L_3 edges), the spin of the electron in the intermediate state is no longer a conserved quantity and therefore spin-exchanging processes can occur. It should be mentioned, however, that the first evidence of magnetic excitations in RIXS came from Cu K edge RIXS measurements[4] although there no single magnon excitation could be space detected because the $1s$ intermediate state of Cu is not spin-orbit split. The RIXS sensitivity to single and higher-order magnetic excitations turned out to be extremely useful in the study of high temperature superconductors, namely cuprates, at the Cu L_3 edge, i.e. in the soft X-ray energy range[5] (as shown in Figure 1.4). Compared to inelastic neutron scattering, RIXS has a poorer energy resolution and low energy features are difficult to resolve. On the other hand, the ease of RIXS in measuring high-energy excitations and the larger cross-section compared to neutron scattering, made it possible to study magnetic excitations in a number of doped compounds, in a way complementary to previous neutron studies.

Similarly to the case of cuprates, RIXS has also been used to probe magnetic excitations in Sr_2IrO_4 at the Ir L_3 edge, i.e. in the hard X-ray energy range[6]. The dispersion and intensity of the single magnon are reported in Figure 1.5.
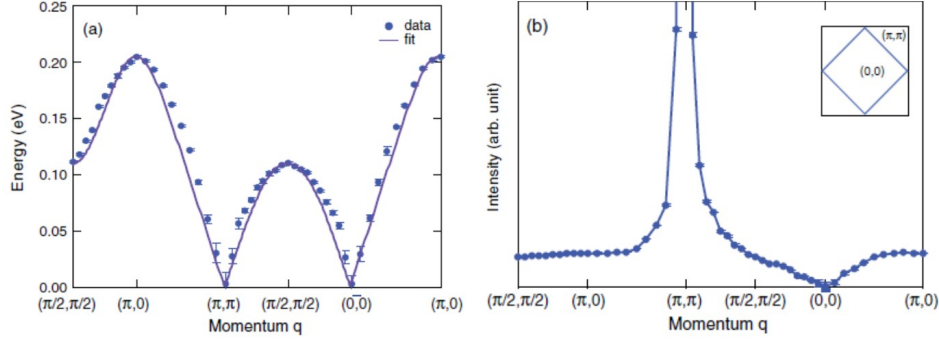
Figure 1.5: (a) single magnon dispersion, (b) the momentum dependence of intensities of Sr_2IrO_4. In both pictures the single points represent the experimental data with the error bars, while the solid line is the fit[6].

The aim of this work is to study the magnetic excitations in $Sr_3Ir_2O_7$ under high pressure with the RIXS technique to provide new experimental evidences for the characterization of the magnetic interactions in this system. This is rather challenging, above all because of the experimental set-up, which is quite difficult to implement, including a Diamond Anvil Cell and a motorised slits unit in a cryostat. To the best of our knowledge, no RIXS measurements of magnetic excitations under pressure have been carried out before.

The magnetic spectrum of $Sr_3Ir_2O_7$ presents two distinct features almost degenerate in energy (within 5 meV or so). With the current energy resolution, these are not well separated. Moreover, one has to mention that the width of magnetic excitations is limited by the instrumental energy resolution and a precise assessment of the intrinsic line width of these excitations is therefore precluded at the moment. Considering that the line width of excitations is related to their life time and ultimately to their decay mechanisms or coupling to other quasi-particle, it would be extremely interesting to assess this quantity. Therefore, part of my work on ID20 was devoted to the conceptual design of new instrumentation aiming at improving considerably the energy resolution of the beam line for magnetic RIXS in iridates. Note that an improvement of the energy resolution would also allow us to study very low energy excitations. Studying phonons at resonance could be very informative on the electron-phonon coupling in the system.

Chapter 2

Experimental set-up

All the experiments concerning this thesis were performed at beam line ID20 of the European Synchrotron Radiation Facility (ESRF), in Grenoble, France. In this chapter the properties of synchrotron radiation and the experimental set-up utilised during the measurements will be described.

2.1 Synchrotron radiation

Synchrotron radiation occurs when charged particles, such as electrons, are accelerated by electromagnetic fields and forced to change their trajectory[7]. If the speed of these particles is sufficiently elevated, close to the relativistic limit, X-rays are emitted.

The principal structures that compose the synchrotron at ESRF are four (see Figure 2.1). In the Linac (linear accelerator), the electrons are "extracted" from a target material, accelerated up to 200 MeV, and injected into the
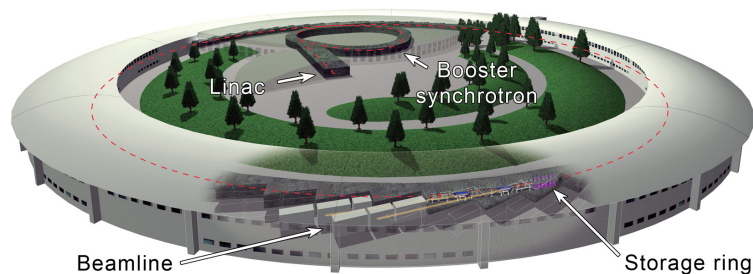
Figure 2.1: Sketch of the ESRF: the LINAC, the booster synchrotron, the storage ring, and a beam line are shown[7].

7
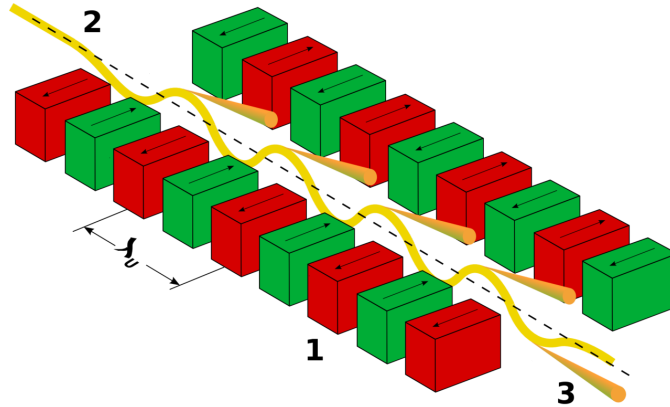
Figure 2.2: Undulators: the electron beam passes through two arrays of magnets, which forces it to change its trajectory emitting radiation. The magnets are arranged such that they change direction with a period of λ_u. The wavelength can be selected changing the gap between the two rows of magnets. 1: Magnets, 2: Electron beam, 3: X-rays[7].

booster synchrotron in "bunches". The latter is a 300 m long pre-accelerator, where the electrons are accelerated up to an energy of about 6 GeV. After that, the electrons are injected into the storage ring, which is a tube of 844 m in circumference, kept at the pressure of 10^{-9} mbar, and composed of 32 straight and 32 curved sections.

The trajectory of the electrons is varied by applying a magnetic field through two types of devices: bending magnets and undulators. The former are placed in the curved sections to force the path of the electron to follow the racetrack of the ring, the latter are situated in the straight sections. Undulators (see Figure 2.2) are periodic magnetic structures composed by two arrays of small magnets, which force the electrons to follow a sinusoidal path, emitting radiation. The radiation emitted after each bend constructively interferes, thus enhancing the emission of radiation at specific energies (harmonics).

Specialized beam lines surround the ring and collect the radiation to perform experiments.

In the following, I will briefly list the main characteristics of undulator radiation:

- energy tunability, i.e. the energy of the emitted radiation can be tuned by adjusting the undulator gap, i.e. the distance in between the arrays of magnets (see Figure 2.2). Beam line ID20 can be operated between

4 and 20 keV;

- high photon flux, i.e. the number of photon produced per unit time is very large. On ID20, the photon flux at the sample is in the order of $\sim 10^{13}$ photons/s;

- high brilliance, i.e. the photon flux normalized to the source area, angular divergence and energy bandwidth, implying highly collimated and partially monochromatic radiation;

- the undulator radiation is naturally polarised in the plane of the electron oscillations;

- the radiation is produced by each "bunch" of electrons, implying a certain time structure of the photon flux. This can be used to perform time-resolved experiments, with resolutions down to 100 ps.

In order to perform resonant inelastic X-ray scattering experiments, high photon flux, photon energy tunability and polarisation control are necessary. It is therefore understandable why the advent of third generation synchrotron radiation has boosted this technique enormously.

2.2 Beam line ID20 at ESRF

ID20 is one of the flagship beam lines of ESRF, constructed in the Phase I of the ESRF Upgrade and operational since summer 2013. It operates in the hard X-ray regime, with photon energies from 4 keV to 20 keV. The studies performed at this beam line concern the investigation of the electronic structure of materials by means of resonant and non-resonant X-ray scattering. As the two techniques have different experimental requirements, two dedicated spectrometers have been installed at the beam line. In the following, I will concentrate on the description of the set-up that we used to perform RIXS measurements.

The source of beam line ID20 is composed of 4 undulators with 26 mm periodicity. However, X-rays from the source need to be further monochromatised and the beam needs to be shaped in order to achieve the required characteristics in terms of energy resolution and spot size at the sample position. For this reason, the beam line comprises a number of optical elements, mirrors and monochromators.

The beam line layout is presented in Figure 2.3. The first optical component is a collimating mirror (CM1), which has a cylindrical shape and collimates the beam in the vertical direction. The vertical divergence of the beam, initially in the order of 15 μrad, is reduced to $\sim$ 2 μrad rms, mostly due to the manufacturing surface errors (slope errors) of the optical element (in the order of 1 μrad).

Downstream CM1 is the Kohzu monochromator, a liquid-nitrogen-cooled double crystal monochromator, based on two silicon crystals both exploiting the (111) reflection. The two crystals are kept at a temperature of about 100 K in order to minimize heat load effects, which would otherwise degrade its performances. Indeed, in the hard X-ray energy range, monochromatisation of the radiation is achieved by exploiting the Bragg reflection of a crystal. According to Bragg's law[8], the wavelength (energy) can be related to the diffracting angle as:

$$n\lambda = 2d\sin\theta_B \tag{2.1}$$

where λ is the wavelength of the beam, d is the distance between the lattice planes, θ_B is the Bragg angle (*i.e.* the angle of incidence of X-rays with respect to the surface) and n is the diffraction order. By fixing the Bragg angle it is possible to monochromatize the beam to a certain energy, by using:

$$E = \frac{hc}{2d\sin\theta_B} \tag{2.2}$$

where h is the Planck's constant and c is the velocity of light in vacuum. Note that d depends on the material and on the reflection order as follows

$$d = \frac{a_{\text{Si}}}{\sqrt{H^2 + K^2 + L^2}} \tag{2.3}$$

where $a_{\text{Si}} = 5.43$ Å is the lattice parameter of Si and H, K, and L are the Miller indices.

According to the kinematical theory of diffraction, only one energy is reflected once the Bragg angle is fixed. However, this is not entirely correct and, as predicted by dynamical diffraction theory, reflection occurs within a distribution of angles with finite width, the so-called Darwin width $\Delta\theta_{\text{DW}}$, which can be expressed as

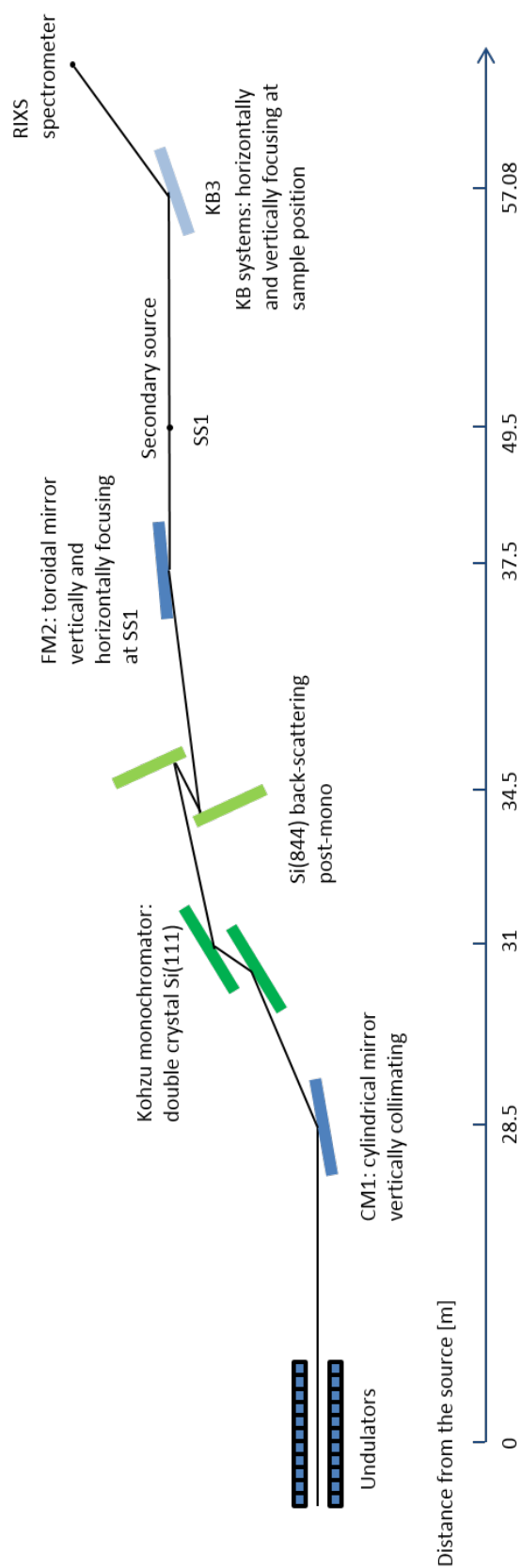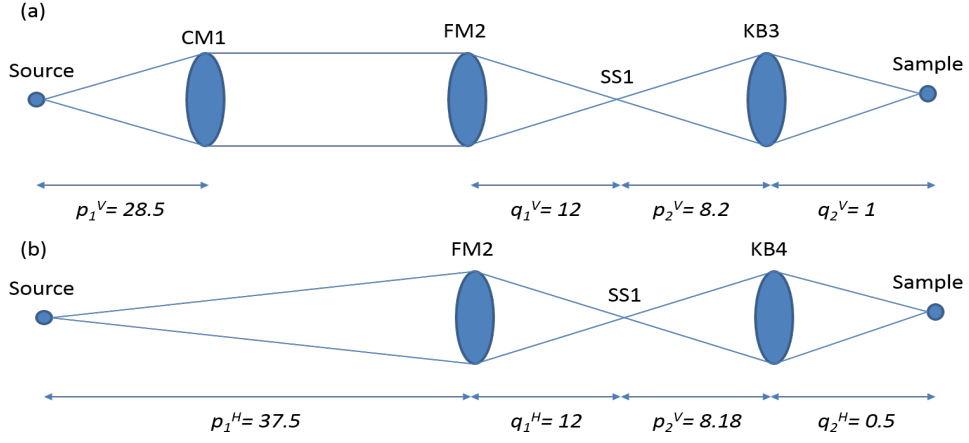$$\Delta\theta_{\text{DW}} = \left(\frac{\Delta E}{E}\right)\tan\theta_B \tag{2.4}$$

Figure 2.3: ID20 beamline at the ESRF.

Figure 2.4: Vertical (a) and horizontal (b) ray paths for the ID20 beam line. Lengths are in meters.

where $\Delta E/E$ is the intrinsic energy resolution of a given reflection. In the case of Si(111) reflection, $\Delta E/E \sim 1.35 \cdot 10^{-4}$. The energy resolution provided by the Si(111) monochromator is easily calculated to be ~ 1.5 eV at 11215 eV. For most RIXS experiments, however, a better energy resolution is required. In the case of Ir L_3 edge RIXS, the energy resolution can be dramatically improved by an additional monochromator, usually called channel-cut, that exploits two Si(844) reflections. As for Si(844) $\Delta E/E \sim 1.3 \cdot 10^{-6}$, one obtains $\Delta E \sim 15$ meV.

At this stage the radiation is monochromatic, but the beam is horizontally divergent and has a size of about 0.4 x 1 mm. It needs to be focused at the sample position. This is done in two steps. First, a toroidal mirror (FM3) focuses the beam both vertically and horizontally at an intermediate position along the beam line. The size of the beam here is ~ 40 x 250 μm (V x H). This point acts as a secondary source (SS) for the optical elements which follow. In particular, a system of Kirkpatrick-Baez mirrors is used to further reduce the size of the beam at the sample position down to ~ 8 x 16 μm (V x H). In the following, I report the formulas to calculate the bending radii of the mirrors, both for meridional and sagittal focus, as well as to estimate the beam size and divergence. Table 2.1 reports the parameters of the optical elements of ID20 beamline. The meridional radius R can be calculated by

$$\frac{1}{p} + \frac{1}{q} = \frac{2}{R\sin\theta} \tag{2.5}$$

Optical elements parameters.				
Optical element	Source-distance [m]	Curvature radius [km]	Dimensions [mm^2]	Slope error [μrad^2 rms]
CM1	28.5	18.4	800 x 80	1 x 10
FM2	37.5	7.7 (V) 5.6 $\cdot 10^{-5}$ (H)	500 x 100	0.7 x 10
KB3	57.17	436 $\cdot 10^{-5}$	300 x 50	0.7 x 10
KB4	57.68	436 $\cdot 10^{-5}$	500 x 50	1 x 10

Table 2.1: Optical elements parameters.

Source parameters	
Spatial shape (V x H)	10 x 400 μm^2 rms
Angular distribution (V x H)	6 x 10 μrad^2 rms

Table 2.2: Source parameters.

Focus and divergence results		
	Focus (V x H) [μm^2]	Divergence (V x H) [μrad^2]
SS1	5 x 130	13 x 34 rms
Sample position	0.6 x 8	100 x 570 rms

Table 2.3: Calculated focus and divergence at the sample position.

where p and q are the source-to-mirror and mirror-to-image distances respectively and θ is the angle of incidence. Instead, the sagittal radius r can be calculated by

$$\frac{1}{p} + \frac{1}{q} = \frac{2\sin\theta}{r}.\tag{2.6}$$

The source parameters are $h = 10$ x 400 μm^2 (V x H) for the beam dimension and $\sigma = 10$ x 6 μrad^2 for the divergence (see Table 2.2). Mirrors act like lenses, and p and q define the magnification ratio, $M = q/p$. The source size and divergence are therefore modified at the image position according to

$$h' = M_1 M_2 h \tag{2.7}$$

$$\sigma' = \frac{\sigma}{M_1 M_2} \tag{2.8}$$

where $M_1 = q_1/p_1$ and $M_2 = q_2/p_2$ are the magnifications defined by the mirror-to-image and source-to-mirror distances, respectively. In the vertical direction only the mirrors FM2 and KB3 are considered, since CM1 only acts to collimate the beam. Thus, $M_1^V = 0.42$ and $M_2^V = 0.13$, and so $h'_V = 0.61$ μm and $\sigma'_V = 0.1$ mrad.

In the horizontal direction, instead, only the toroidal mirror and the second KB mirror should be considered and the magnifications are $M_1^H = 0.32$ and $M_2^H = 0.06$. Thus $h'_H = 7.7$ μm and $\sigma'_H = 0.57$ mrad (see Table 2.3). According to these calculations, the beam size at the sample position turns out to be largely underestimated. Indeed, we are considering only geometrical contributions and neglecting all the possible sources of beam broadening. In particular, the surface errors of optical elements (slope errors) entirely determine the spot size in the vertical direction, as it can be seen in the Shadow simulations (see Section 4.2).

2.3 RIXS spectrometer

The RIXS spectrometer at ID20 beam line, is shown in Figure 2.5. Diced spherical crystal analysers are used to characterise the radiation scattered by the sample in terms of energy and momentum transfer. These are mounted on a movable arm, such that the scattering angle can be varied both in the horizontal and vertical plane.

The energy resolution is obtained by exploiting the Bragg reflection of crystal
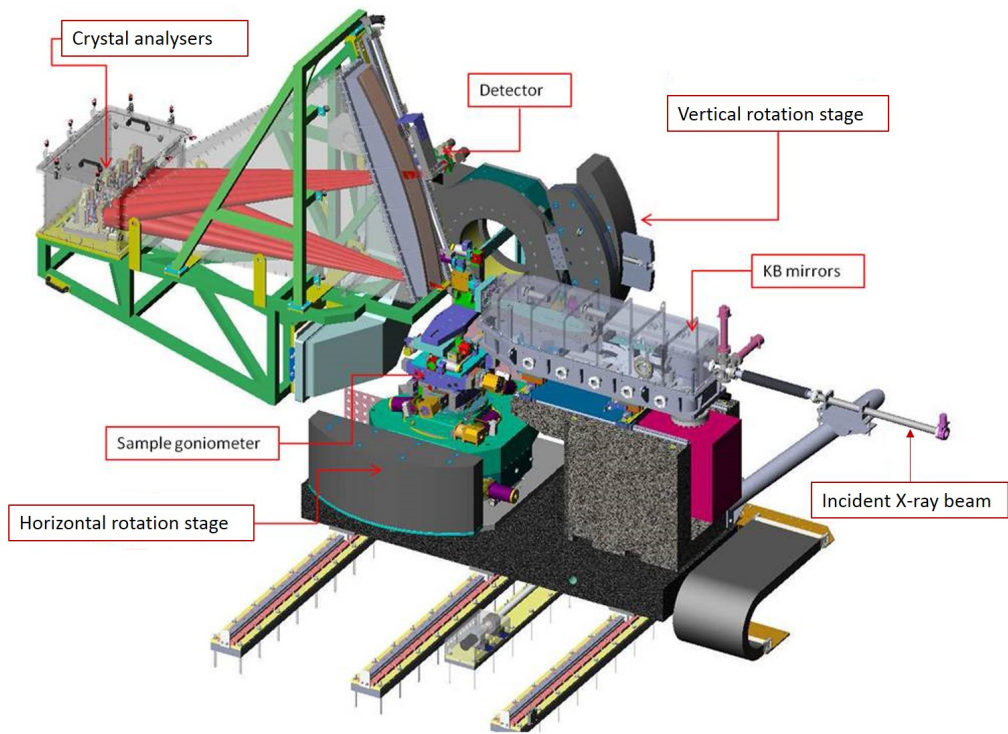
Figure 2.5: The RIXS spectrometer.
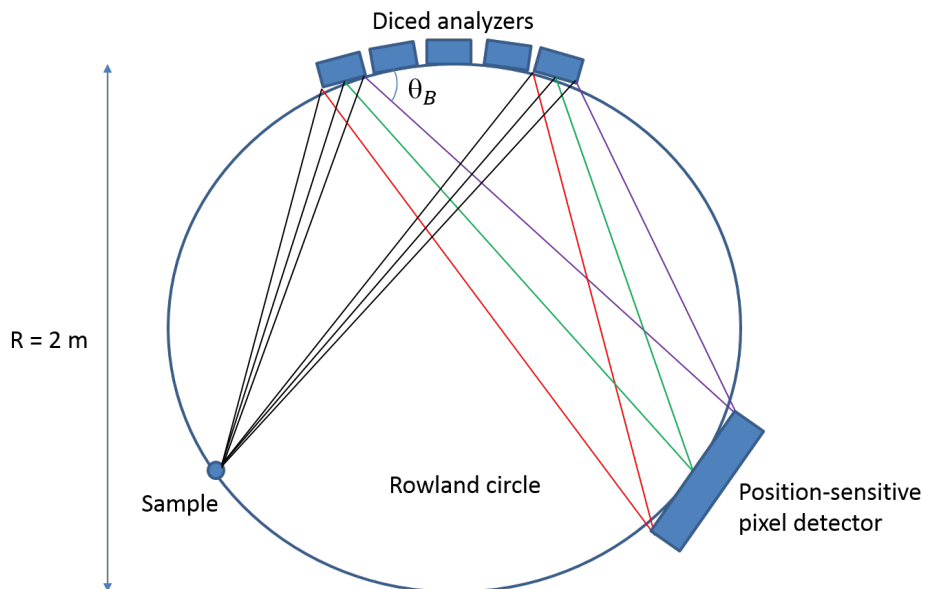
Figure 2.6: Rowland circle geometry, where θ_B is the Bragg angle and R is the diameter of the circle.

analysers. These are arranged in the Rowland circle geometry, such that the sample acts as the source and the image is formed at the detector position. The radius of curvature of the analysers is chosen in order to satisfy the focusing condition. In the case of Ir L_3 edge RIXS experiments, spherical (R=2 m) diced crystal analysers exploiting the Si(844) reflection are used. Here a perfect single crystal is cross-grooved to form an array of several individual cubes, arranged on a spherical surface[9, 10, 11]. The contribution of different dices superimposes at the detector position[12] (see Figure 2.6). When using these crystals close to back-scattering (θ_B close to 90°), the image at the detector is a square with twice the cube size c, i.e. approximately $2c \sim 1.5$ mm.

There are several contributions to the energy resolution of the spectrometer. The first one is the intrinsic energy resolution of the Si(844) reflection, which is $\Delta E_{DW} \sim 15$ meV as in the case of the post-monochromator. Additional contributions to the energy resolution are due to the finite pixel and source sizes. Each wavelength from the sample is reflected by the different dices and focused in the same place on the detector. Thus, there is a well-defined relationship between energy and position of the scattered beam onto the detector. If its pixel size p is $p \ll 2c$, the cubic size contribution is replaced by a pixel size contribution[13]:

$$\left(\frac{\Delta E_p}{E}\right) = \left(\frac{p}{2R \sin \theta_B}\right) \cot \theta_B. \tag{2.9}$$

The second geometrical contribution to the resolution is the finite source size s, which can be calculated as:

$$\left(\frac{\Delta E_s}{E}\right) = \left(\frac{s}{R \sin \theta_B}\right) \cot \theta_B. \tag{2.10}$$

At the Iridium L_3 edge the various contributions amount to[12]:

- analyser intrinsic Darwin width: $\Delta E_{DW} = 15$ meV

- finite source-size s contribution: $\Delta E_s = 6.3$ meV for $s = 15$ μm

- pixel-size p contribution: $\Delta E_p = 11.5$ meV for $p = 55$ μm
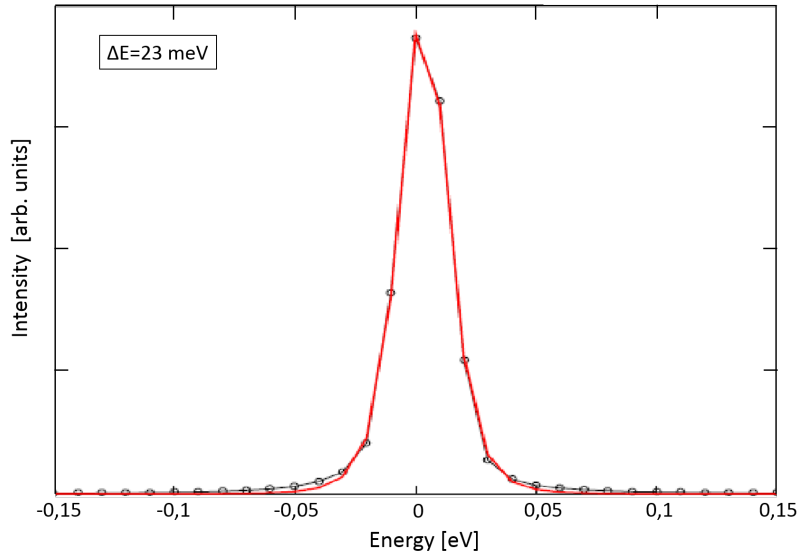
Figure 2.7: Overall energy resolution for the Ir L_3 edge set-up as determined by elastic scattering from a 40 μm thick polymer film. Experimental data (black line) and fit to the data (red line).

The energy resolution of the spectrometer is then:

$$\Delta E_{spec} = \sqrt{(\Delta E_{DW})^2 + (\Delta E_s)^2 + (\Delta E_p)^2} = 20 \text{ meV} \qquad (2.11)$$

To calculate the overall energy resolution one has to take into account also the resolution of the incoming beam, ΔE_i, which is 15 meV. So the final resolution of the collected spectra is:

$$\Delta E_{tot} = \sqrt{(\Delta E_{spec})^2 + (\Delta E_i)^2} = 25 \text{ meV} \qquad (2.12)$$

This value closely matches the one observed experimentally (see Figure 2.7), implying that we have a good understanding and control of the energy resolution of the beam line and the spectrometer.

Chapter 3

High pressure RIXS measurements

The main purpose of these experiments is to study the behaviour of magnetic excitations in iridates, $Sr_3Ir_2O_7$ in particular, at high pressures (up to 6 GPa) and low temperatures (down to 150 K) by RIXS. The motivation behind this experimental effort is that the description of magnetic excitations in this compound has been ambiguous and is not completely understood so far; indeed, at least a couple of magnetic models have been proposed to describe the magnetic excitation spectrum of this system. By applying pressure, we intend to study the response of magnetic excitations to external stimuli and provide new experimental evidences to test these theories.

In Section 1 of this chapter the electronic, crystallographic and magnetic properties of $Sr_3Ir_2O_7$ will be described; then (Section 2) the experimental set-up will be described and finally (Section 3) the RIXS spectra will be analysed and discussed.

3.1 Sample description

In this section the main physical properties of $Sr_3Ir_2O_7$ are presented. In particular, the electronic and magnetic structure are shown in detail, as they are of pivotal importance to understand our RIXS measurements (which will be described in Section 3 of this chapter). This is the very first RIXS measurement in which a single magnon excitation has been detected at high pressures.

3.1.1   Electronic structure

Most of the Transition Metal Oxides (TMOs) can be classified as strongly correlated materials. The electronic properties of these systems, at least for $3d$ TMOs, can be successfully described by the Hubbard model, which can be considered as a development of the tight-binding model. The two main terms in the Hubbard Hamiltonian are the hopping integral t, which is related to the kinetic energy and is proportional to the overlap between orbitals (W), and the Coulomb repulsion of two electrons occupying the same site (U). These two parameters help to discriminate between the insulating or metallic behaviour of a specific material. Indeed if $U \ll W$ the energy cost related to the repulsion between two electrons is lower than the gain in kinetic energy and thus electrons are free to move inside the material, which is therefore metallic. Instead if $U \gg W$ the electron-electron repulsion is strong enough to forbid any hopping and the material is an insulator. Moving towards heavier transition metals, such as the $4d$ and $5d$ TMOs, the electron-electron interaction is expected to become less important, while the hopping integral is expected to increase, because of the larger spatial extension of these orbitals compared to the $3d$ ones. This should lead to a metallic state. Instead several iridate compounds, such as some members of the Ruddlesden-Popper series ($Sr_{n+1}Ir_nO_{3n+1}$), are found to be insulating, in particular Sr_2IrO_4 and $Sr_3Ir_2O_7$ (n=1 and n=2 respectively)[14, 15]. To explain this unexpected insulating characteristic the Spin Orbit Coupling (SOC) must be taken into account in the calculation of the ground state[16, 17]. Here this theory (called $J_{\text{eff}} = 1/2$) will be described for the compound of our interest, $Sr_3Ir_2O_7$. In the crystal, the Ir ions are tetravalent and their electronic configuration is $[Xe]4f^{14}5d^5$, thus their outermost shell is half-filled. Each Ir ion is surrounded by an octahedron of O ions. The electric field felt by the Ir $5d$ electrons is therefore due to the resulting positive charge of the nucleus plus the inner shells and to the negative charges due to the O ions. The symmetry of this electric field is not spherical but cubic, leading to the splitting of the $5d$ orbitals into t_{2g} and e_g states. In fact, since the most external electrons in the Ir atoms feel the negative charges of the surrounding oxigens, the e_g orbitals, which point directly to these charges, are energetically higher, while the t_{2g}, pointing between the negative charges, lie at lower energies. In this configuration the e_g band is completely empty, while the t_{2g} band is partially filled. The Coulomb repulsion is too small
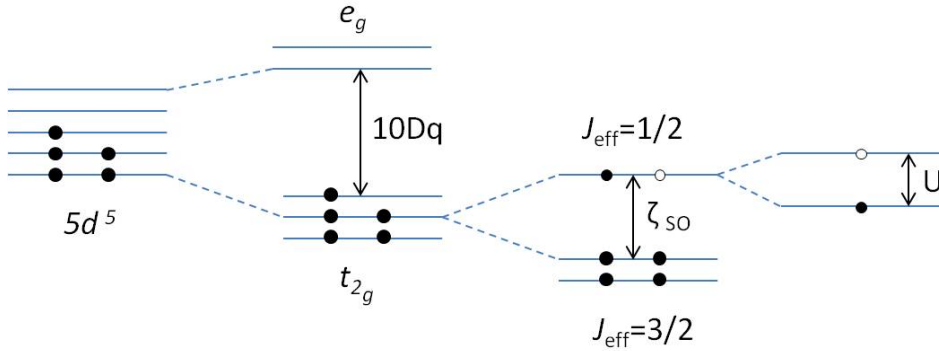
Figure 3.1: Energy levels of the $J_{\text{eff}} = 1/2$ theory.

with respect to the cubic crystal field (which is in the order of ~ 3 eV), thus a metallic state is expected. One has also to consider the role of SOC, which is large in $5d$ elements. If the SOC is considered ($\zeta_{SO} \sim 0.4$ eV), the t_{2g} levels are split into a doublet band at higher energies called $J_{\text{eff}} = 1/2$ and a quartet low energy band called $J_{\text{eff}} = 3/2$. The quartet level is completely filled and the doublet is half-filled. Since both the cubic crystal field and the SOC reduce the $5d$ bandwidth into an "effective" bandwidth (the one of the $J_{\text{eff}} = 1/2$ band), even a small Coulomb repulsion U can act to open a gap and the insulating behaviour is explained. This is summarised in Figure 3.1. Actually, since the O octahedra are elongated along the c axis, there is a further reduction in the symmetry of the electronic field felt by the Ir outermost electrons. This can be taken into account by considering a tetragonal crystal field, which further splits the energy levels[18]. The pure $J_{\text{eff}} = 1/2$ ground state is strictly achieved if no tetragonal distortion is considered.

3.1.2 Crystal structure

$Sr_3Ir_2O_7$ single crystals were grown for the first time by R. S. Perry, E. C. Hunter, D. Prabhakaran and A. T. Boothroyd at the London Center for Nanotechnology (University College London) and the Clarendon Laboratory (University of Oxford) using the flux technique[20]. The crystal structure is shown in Figure 3.2. The space group of this compound was first suggested to be I4mmm[20] but it was then proved to be $Bbcb$ by H. Matsuhata *et al.*[21]. $Sr_3Ir_2O_7$ has a layered perovskite structure, which consists in
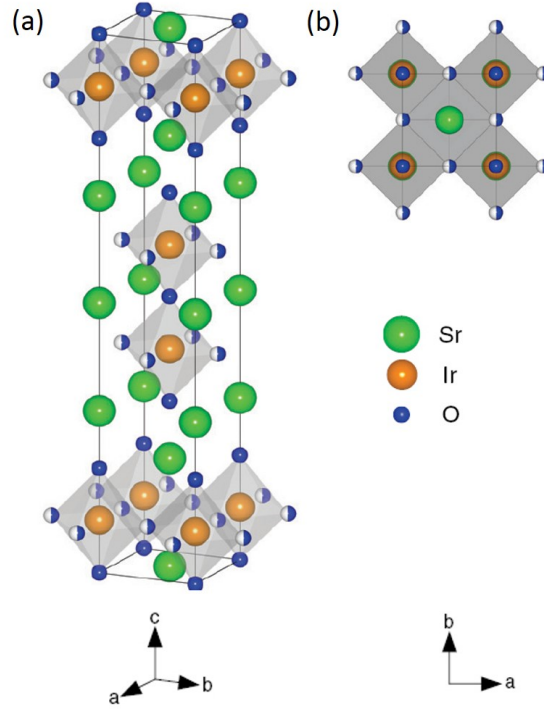
Figure 3.2: Side (a) and top (b) view of the $Sr_3Ir_2O_7$ unit cell[19].

blocks of bilayers formed by corner-sharing IrO_6 octahedra, alternated with SrO planes. The octahedra are elongated along the c direction by $\simeq 1.6$ % with respect to the in-plane Ir-O distance; they are also rotated around the c axis by an angle of $\simeq 11°$ in a staggered way so that the Ir-O planes in each bilayer are slightly out of phase with each other[15]. The IrO_2 planes and the octahedral coordination of Ir make this structure very similar to that of the cuprates semiconductors.

3.1.3 Magnetic structure and previous experiments of magnetic excitations

$Sr_3Ir_2O_7$ is a weak G-type antiferromagnet at low temperature ($T_N \sim 230$ K); the magnetic structure consist of two antiferromagnetic domains, as shown in Figure 3.3, in which the magnetic moments align along the c axis. Each Ir ion has a magnetic moment of $\boldsymbol{\mu} = 0.037\mu_B/$Ir with an applied magnetic field of 7 T at the temperature of 2 K[22]. If field-cooled $Sr_3Ir_2O_7$ shows two transitions at 285 K and 260 K, resulting in an increase of the magne-
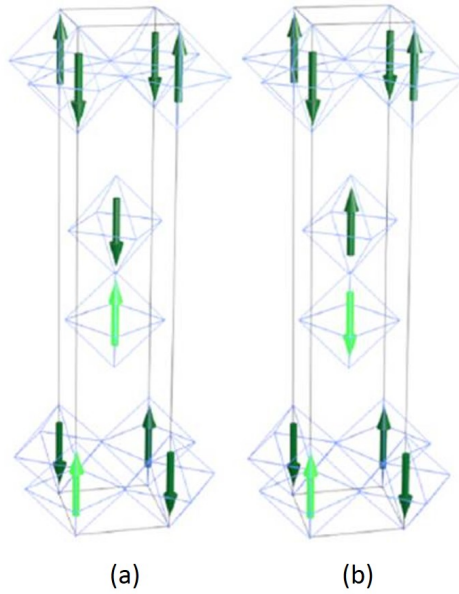
Figure 3.3: The two possible magnetic structures of $Sr_3Ir_2O_7$, (a) and (b)[22].

tization; however, below 50 K a rapid drop occurs, and the magnetization assumes a negative value (due to the opposite orientation of the magnetic moments with respect to the magnetic field)[15, 22].

While the previous magnetic properties seem to be unanimously well understood, a theory which fully explains the magnetic excitations in this compound is totally missing. Previous measurements of spin excitations have been performed at room pressure with the RIXS technique by J. Kim *et al.*[23]. They observed a giant magnon gap of $\sim$ 90 meV both for the optical and acoustic branches, which can not be explained by the Heisemberg model, and a small bilayer splitting ($\sim$ 5 meV) between the two branches observed at different L. These results are shown in Figure 3.4: the magnetic feature (B) is clearly present at energies of $\sim$ 90-100 meV, and it is most intense at $(H, K){=}(\pi, \pi)$, proving the existence of a large gap at least for the optical mode. To investigate the acoustic mode, which seemed to be absent, measurements has been made at different L. As proposed by D. Reznik *et al.*[24], in fact, the cross sections of the magnetic optical and acoustic excitations in these compounds follow an opposite behaviour with respect to L, as will be explained later in this chapter. Thus the small observed bilayer splitting between $L = 0$ and $L = \pi$ was interpreted as due to almost degenerate acoustic and optical magnetic branches (see Figure 3.4(b)).
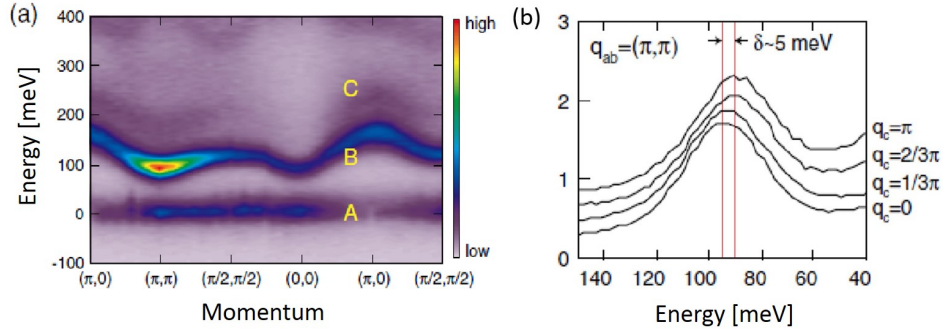
Figure 3.4: RIXS data of single magnon excitation in $Sr_3Ir_2O_7$ along high symmetry lines of the Brillouin zone (a) and selected RIXS spectra at (π, π, L) showing the bilayer splitting (b)[23].
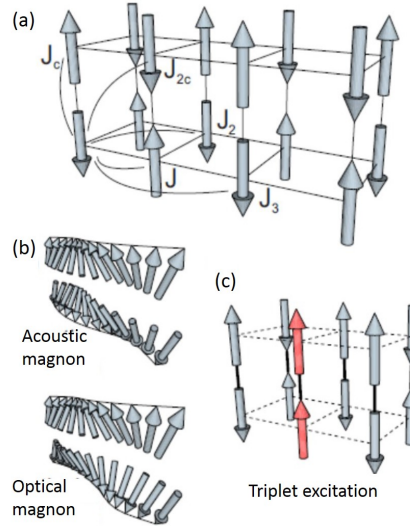

Figure 3.5: (a) the intra- and inter-layered coupling, (b) acoustic and optical modes described in the first theory, (c) dimer triplet excitation found in the second theory[25].

Recently, however, further measurements were performed on $Sr_3Ir_2O_7$ that highlighted the presence of an additional feature, undetected previously, which raised doubts on the previous interpretation of the magnetic excitation spectrum of $Sr_3Ir_2O_7$ and, ultimately, of its magnetic ground state. Indeed, an alternative theoretical model has been put forward that moves from a completely different approach. In the first model, inter-layer coupling is considered to be small compared to the intra-layer coupling ($J_c \ll J$, see Figure 3.5(a) for a definition of the magnetic couplings) and therefore the ground state is a long-ranged ordered Nèel-like state and the magnetic excitations are conventional spin-waves in the presence of strong anisotropy which induces a large magnetic gap. In the latter model, on the contrary, the authors considers the possibility that $J_c \gg J$, which produces a dimerised ground state. In the absence of anisotropy, this would be a disordered collection of singlets with no staggered magnetization and the magnetic excitations would be naturally gapped (singlet-triplet excitations). Anisotropy also needs to be included here, however, to explain the finite staggered magnetization which is experimentally observed in this compound. The idea is then to study these excitations with the RIXS technique under high pressure to provide new experimental evidences to test these theories.

3.2   Experimental details

In this section the high pressure experimental set-up is described. Many devices were utilized in order to reach the temperature and the pressure needed and to acquire the signal from the sample without any spurious contribute. To reach the desired pressure the sample must be placed between the two diamonds of a Diamond Anvil Cell (DAC) (shown in Figure 3.6). Here one of the two diamonds can be pushed against the other (which is kept fixed) by a membrane which expands or shrinks according to the quantity of He gas injected by a pump, which can be controlled manually. It is important to keep the pressure isotropic (and not uni-axial) on the sample since a lack of pressure uniformity could deteriorate the sample and lead to an inconsistent data acquisition. To do so, the sample is surrounded by a gas (He) which is kept between the diamonds by a ring (the gasket) placed in-between them. Since the gasket material must be as transparent as possible to X-rays, we have chosen to utilise Beryllium. This unfortunately leads to other incon-
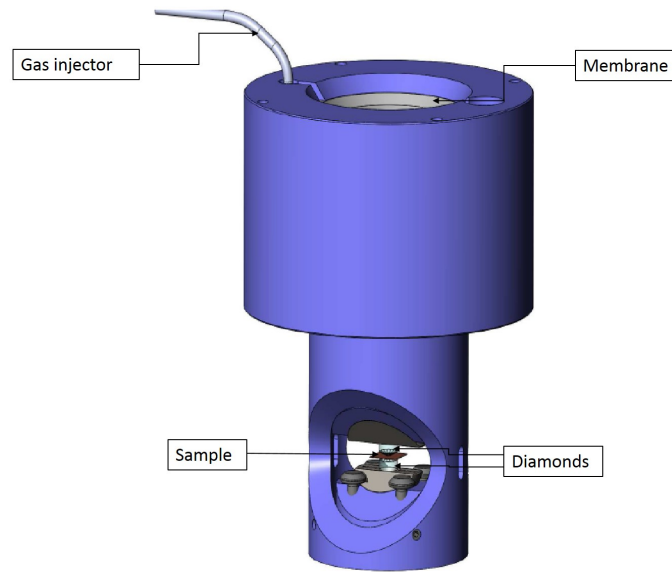
Figure 3.6: Diamond Anvil cell.

veniences regarding the scattering geometry which will be discussed later in this Section. The complete sample environment is shown in Figure 3.7.

To measure the exact pressure on the sample a Pressure by Ruby Luminescence system (PRL) was utilized (see Figure 3.8). This system in fact permits to determine the exact value of the pressure applied in-situ, while to operate only on the gas injector could lead to some errors. More precisely, a laser beam, coming from the PRL, illuminates a ruby placed very close to the sample (see Figure 3.7) and excites luminescence. Since the energy positions of the ruby luminescence peaks are very well known as a function of pressure, this allows determining the exact value of the pressure acting on the ruby, and thus on the sample.

It is fundamental that during the experiment the whole chamber hosting the DAC is kept in vacuum: this is necessary to prevent scattering from air. Moreover, since the magnetic excitations are visible only at $T < T_N$, a Liquid Nitrogen Cryostat (see Figure 3.9) is required to reach the desired temperature, which in this case was chosen to be 150 K.

As reported before, one of the main problems in this set-up was the presence of the Be gasket. This causes elastic and inelastic scattering, which could lead to spurious peaks in the spectra, obscuring the signal of the sample. For this reason it has been chosen to work with a scattering geometry at $2\theta \sim 90°$
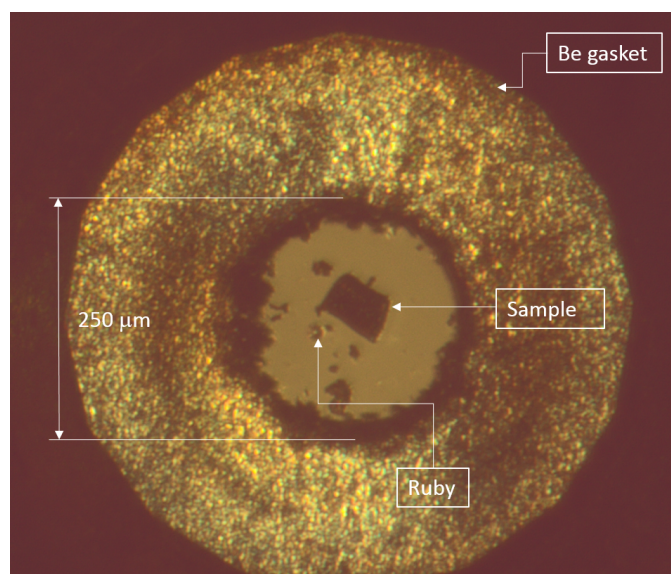
Figure 3.7: Be gasket with a diameter of 250 μm in the middle of which the sample and the ruby are placed.
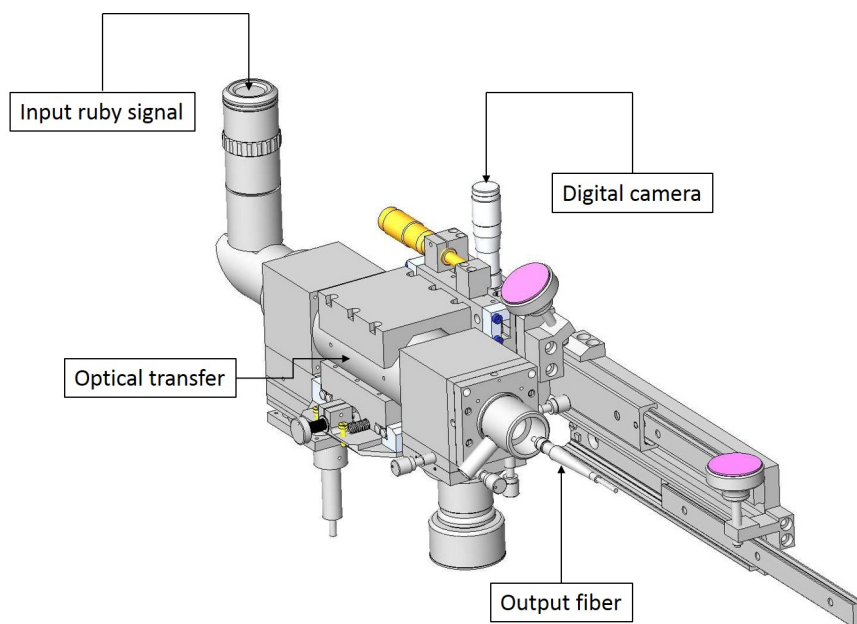
Figure 3.8: Pressure by Ruby Luminescence system.
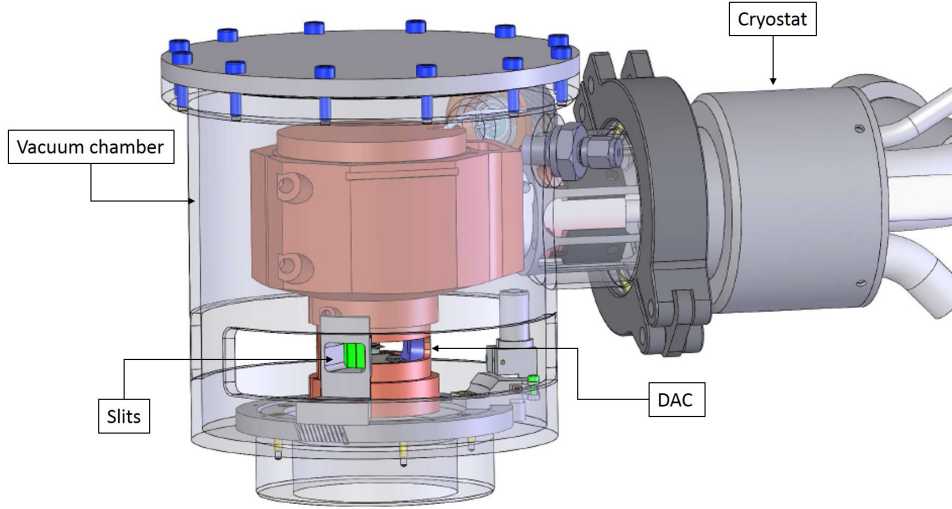
Figure 3.9: The complete environment of the high pressure cell, comprising the vacuum chamber, the cryostat and the slits.

in the horizontal plane (see Figure 3.10), for which all the elastic contribution from the Be was eliminated, due to the $\epsilon_1 \cdot \epsilon_2$ polarisation term, which in this case is equal to zero at 90°. Nevertheless the small contribution from the Be is not negligible because of the finite collecting solid angle. For this reason a motorised slit unit was installed inside the vacuum chamber close to the DAC, in order to geometrically limit the signal coming from the Be and reaching the analyser (as it can be seen in Figure 3.10). The motorised slit and the analyser mask reduce the collecting solid angle in narrow angular range close to 90°, forming a proper collimating system. Following simple geometrical consideration, it is possible to calculate the field of view of the analyser (red dashed line in Figure 3.10) as:

$$f = s + a \, \frac{A + s}{L + a} \tag{3.1}$$

where $s = 80$ μm is the aperture of the slit, $a = 16$ mm is the distance between the slit and the sample, $A = 15$ mm is the width of the mask and $L = 1.97$ m is the distance between the mask and the sample, as shown in Figure 3.10. It turns out that the portion of Be that the analyser sees is only 200 μm and from the region of space closest to 90°. A test experiment for the slits was made, as shown in Figure 3.11. As can be seen, the slits remove most of the signal coming from the Be, which would otherwise completely
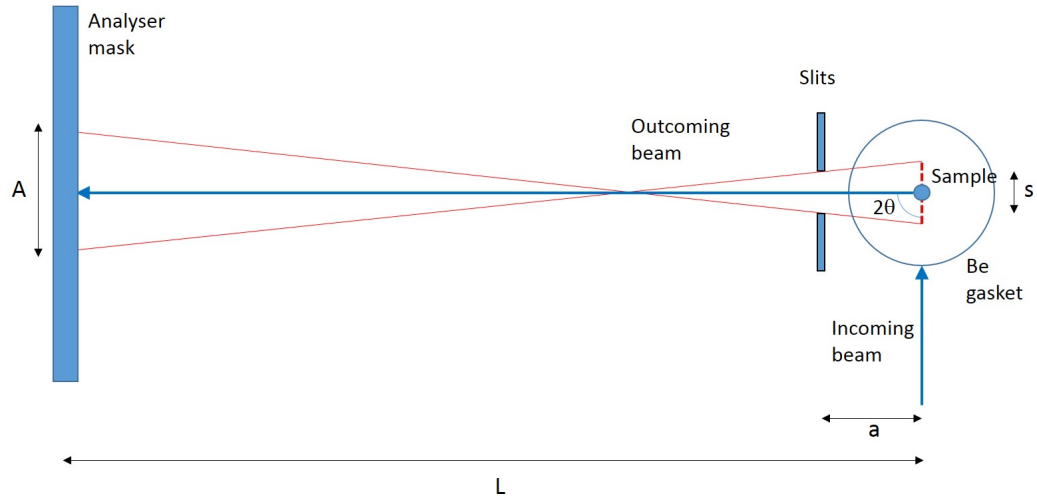
Figure 3.10: Scattering geometry showing the position of the slits with respect to the sample, the Be gasket, and the analyser mask.
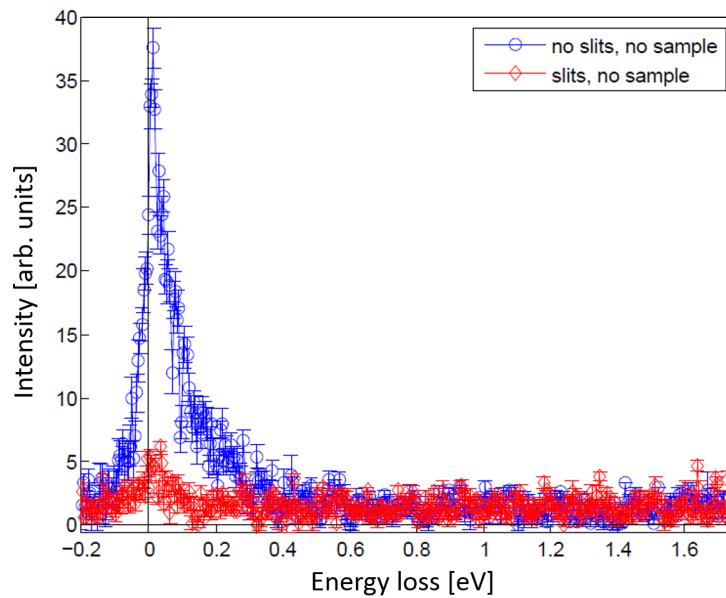
Figure 3.11: RIXS spectra acquired using the slits (red diamonds) and without them (blue circles). The slits clearly eliminate most of the Be contribution.

cover the magnetic scattering signal from the sample.

3.3 Results and discussion

Figure 3.12 shows a RIXS spectrum measured at high pressure (6 GPa). The black circles represent the experimental data, the blue line is the fit of the data, and the red dashed curves are the single features used in the fitting. To perform the fit of the spectra, each feature was modelled using a Pearson type VII distribution:

$$p(\mathbf{P}, x) = \frac{A}{\left(1 + \left(2^{\frac{1}{\mu}} - 1\right)\left(2\frac{x - x_0}{w}\right)^2\right)^\mu} \tag{3.2}$$

where $\mathbf{P}$ is the vector whose elements are the fit parameters, i.e. the amplitude of the curve, A, the peak centre, x_0, the full width half maximum (FWHM), w, and the parameter μ which adjusts the shape of the curve (in particular if $\mu = 1$ the curve has a pure Lorentzian shape, while if $\mu \to \infty$ it has a pure Gaussian shape). All these parameters were adjusted to better reproduce the experimental data. It must be noticed that four different features are present in all the spectra acquired (shown in red in Figure 3.12): the elastic peak at $E = 0$, an intense feature at ~ 100 meV, which is the magnetic excitation, a broad feature at slightly higher energies, which could be interpreted as a bimagnon, and another feature which is common in iridates and represents an intra-t_{2g} excitation.

RIXS spectra were measured at different points of the Brilloiun zone and at different pressures, as summarised in Table 3.1. In particular, they were taken at $Q_1 = (\pi, \pi, 0)$, $Q_2 = (\pi, \pi, 1.74)$, $Q_3 = (0, \pi, 0)$, $Q_4 = (\pi/2, \pi/2, 10)$. Figures 3.13 and 3.14 show RIXS spectra measured at Q_1 and Q_2 at pressures of 1, 3, and 6 GPa. The spectra clearly reveal that the energy position of the single magnon changes with pressure. In particular for Q_2 and Q_3 the energy of the magnetic excitation increases with increasing the pressure, while for Q_1 and Q_4 the magnon follows the opposite trend.

In the scenario where the main magnetic feature is dominated by the superposition of degenerate acoustic and optical magnetic branches, it is useful to recall that the dynamic structure factors of the two modes have a periodic
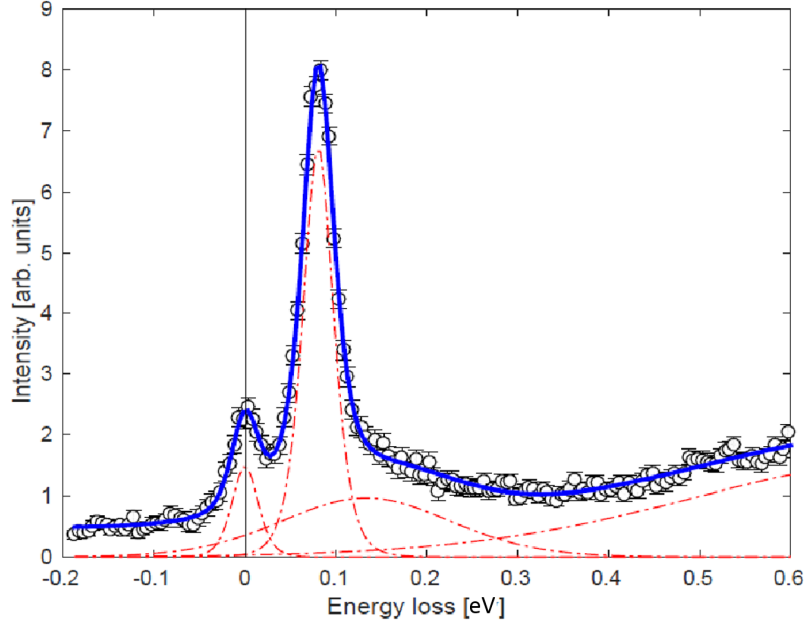
Figure 3.12: The recorded spectrum for the point Q_1 at 6 GPa. The experimental data points are shown in black, the result of the fitting process in blue, and the individual curves used for the fitting are shown as red dashed lines.

Lattice point $(H,\ K,\ L\ )$	Pressures [GPa]	Trend [meV/GPa]
$(\pi,\ \pi,\ 0)$	1 GPa 3 GPa 6 GPa	-1.3
$(\pi,\ \pi,\ 1.74)$	1 GPa 3 GPa 6 GPa	1.4
$(0,\ \pi,\ 0)$	1 GPa 3 GPa 6 GPa	2.5
$(\pi/2,\ \pi/2,\ 10)$	1 GPa 3 GPa 6 GPa	-2.8

Table 3.1: Lattice points with pressures at which they have been measured and trend of the energy magnon peak as the pressure increases.
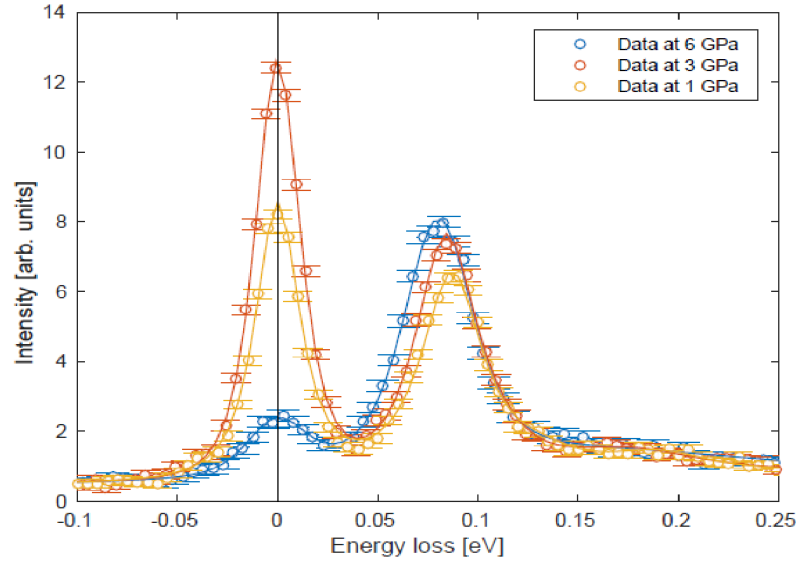
Figure 3.13: RIXS spectra at Q_1 at 1 GPa (yellow), 3 GPa (red) and 6 GPa (blue) in comparison. It clearly results that at high pressures the magnetic excitation moves towards lower energies.
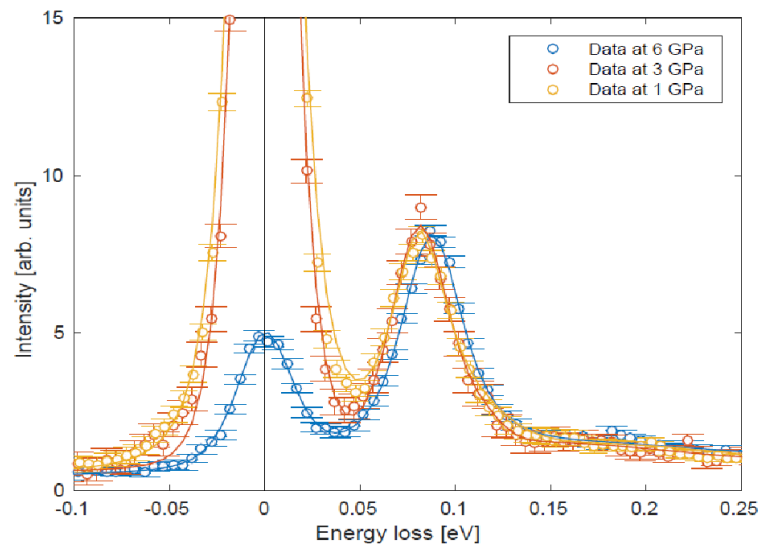
Figure 3.14: RIXS spectra at Q_2 at 1 GPa (yellow), 3 GPa (red) and 6 GPa (blue) in comparison. At high pressures the magnetic excitation moves towards higher energies.
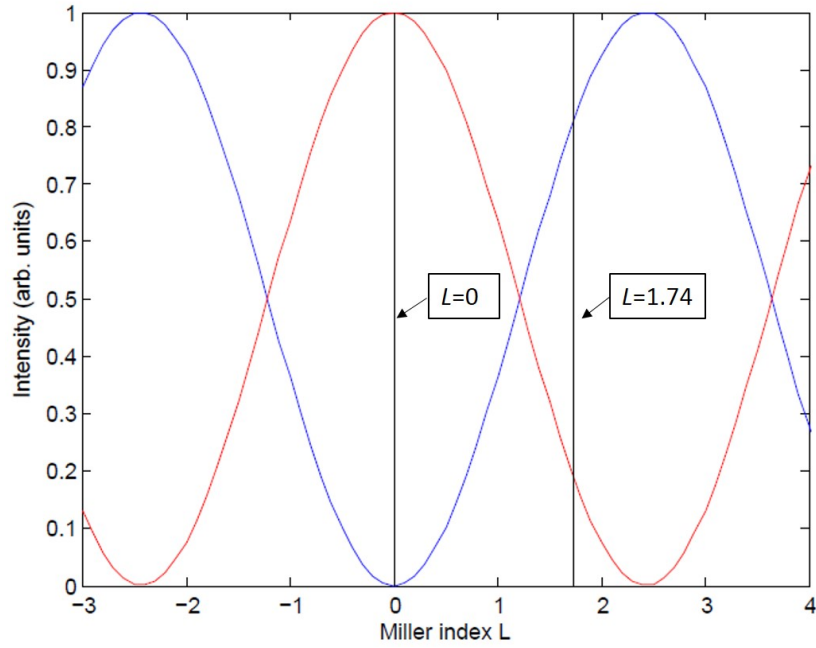
Figure 3.15: The magnetic excitation cross section as reported by D. Reznik *et al.*. It must be noticed that for $L=0$ only the optical mode (red) has spectral weight, while for $L=1.74$ the main contribution is given by the acoustic mode (blue).
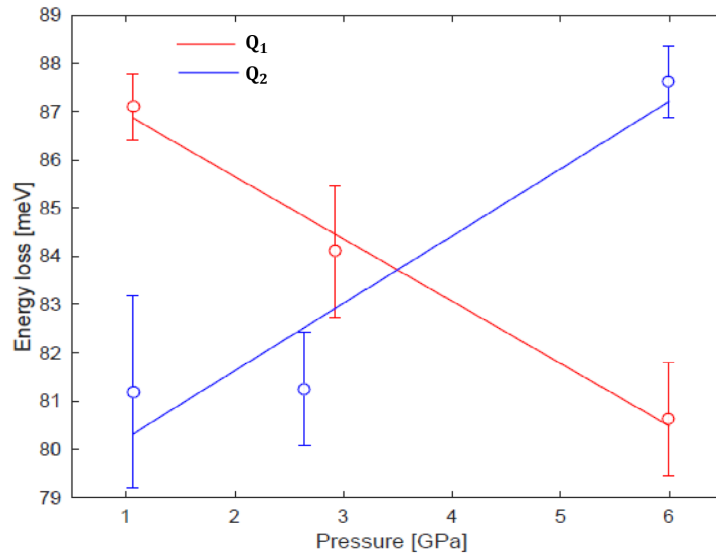
Figure 3.16: Energy dependence of the magnetic excitations as a function of pressure. For $L=0$ (red) and $L=1.74$ (blue) an opposite behaviours is observed. The slope of the fitting lines are respectively -1.3 meV/GPa and 1.4 meV/GPa

dependence on L given by[24]:

$$\left(\frac{\partial^2 \sigma}{\partial \Omega \partial E} \right)_{acoustic} \sim \sin^2 \left(\pi \frac{b}{c} L \right) \tag{3.3}$$

$$\left(\frac{\partial^2 \sigma}{\partial \Omega \partial E} \right)_{optical} \sim \cos^2 \left(\pi \frac{b}{c} L \right) \tag{3.4}$$

where b is the distance between two nearest neighbour Ir magnetic moments within one bilayer and c is the lattice spacing. The two curves are represented in Figure 3.15. The periodicity in L of the oscillations is given by $c/b \sim 5$, whereas the shift between the two curves is such that when the acoustic mode reaches its maximum intensity the optical mode vanishes and vice versa. It is therefore instructive to focus on the points Q_1 and Q_2, since the the RIXS spectra at Q_1 should be purely due to the acoustic mode and that at Q_2 predominantly due to the optical mode. Interestingly, the pressure dependence of the magnon mode at the two transferred momenta is opposite, as it is summarized in Figure 3.16. It is particularly remarkable that the fitting slopes are almost identical: indeed, for $L = 0$ it is -1.3 meV/GPa, while for $L = 1.74$ it is 1.4 meV/GPa.

Thus, it seems that the optical mode moves to lower energies while the pressure increases, while the acoustic mode moves in the opposite direction. This experimental finding may be in favour of the first of the two proposed models, in which an acoustic and an optical modes are almost superimposed, but have different pressure dependences. In the scenario where the main magnetic mode is interpreted as a dimer excitation, it is difficult to explain the L dependence of the pressure effect. On the other hand, we believe that the investigation of magnetic excitations should be pursued at even higher pressure in order to perturb the system to a larger extent.

Chapter 4

An optical scheme to improve the energy resolution: "rainbow" monochromator and spectrometer

As we have seen in the previous chapter, the width of magnetic excitations is often limited by the instrumental energy resolution. Therefore, a precise assessment of their intrinsic line width is not possible at the moment. In this chapter we propose a set-up to achieve an energy resolution in the range of a few meV at the Ir L_3 edge. With this, in fact, it would be possible to separate magnon bunches and excitations lying close in energy. Moreover, the systematic study of the broadening of magnetic excitations provides information on the mechanisms which limit their life time and eventually on their coupling to other excitations, e.g. phonons. Also, an improvement in the energy resolution will also open the way to the study of phonons at resonance, which directly provides information on the electron-phonon coupling in the system[26].

The chapter is organised as follow: we propose a new monochromator (Section 1) based on a dispersive optical element, which we call "rainbow", and estimate its energy resolution contribution. Then (Section 2) we report the results of ray-tracing simulations performed using the SHADOW code[27, 28]. In section 3 and 4 we propose two methods to implement a new spectrometer to achieve the desired energy resolution.
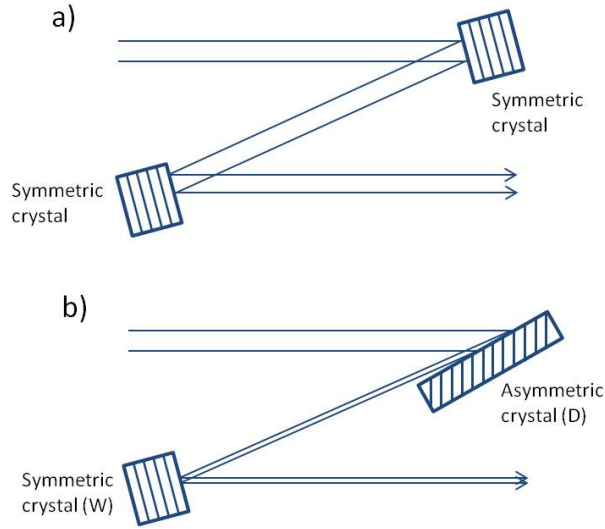
Figure 4.1: (a) monochromator using only Si(844) symmetrical reflection, still used at the beam line, (b) new monochromator set-up, exploiting the asymmetrically-cut Si(844) crystal.

4.1 Monochromator

As already mentioned above, we focus on the improvement of the energy resolution at the working energy of Ir L_3 edge RIXS experiments, i.e. nominally 11215 eV. For the monochromator, we propose a new optical layout based on the CDW concept proposed by Shvyd'ko[29] as shown in Figure 4.1 b). In the CDW configuration there are three active optical elements. C collimates the X-rays in the dispersion plane; in the case of ID20 the radiation is collimated by the first optical element of the beam line (see Section 2.2) and therefore an additional optical element is not needed here; D disperses the beam according to photon energy. In our case this is obtained by using a highly asymmetrically-cut Si(844) crystal, i.e. with the Bragg planes rotated by an angle η with respect to the crystal surface. In symmetrically-cut crystals, the incident and diffracted beam experience the very same refraction effects at the crystal-vacuum interface, which then compensate and cancel out. On the contrary, in asymmetrically-cut crystal, the difference in refraction between the incident and the diffracted beam can be used to shape the beam properties, including the beam divergence. These effects are strongly energy-dependent, and therefore a relationship between angle and energy is established (see Fig.4.2, from which it becomes clear why we use the term
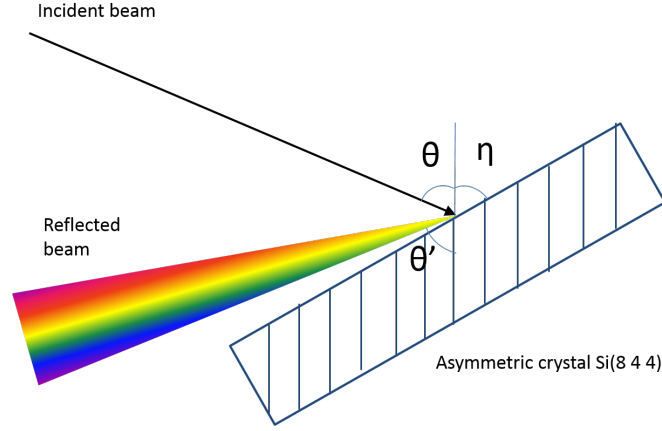
Figure 4.2: The monochromator idea.

"rainbow"); finally W, a wavelength selector, acts as an angular slit and picks up only a fraction of the X-ray fan, thus reducing the overall energy bandwidth. In our case, this can be done by using a symmetrically-cut Si(844) crystal, provided that the angular acceptance of the latter is smaller than the angular X-ray fan introduced by the first crystal. The current set-up is compared to the (C)DW one in Figure.4.1

The most important quantity to evaluate is the angular dispersion rate introduced by the first asymmetrically-cut crystal. This is given by:

$$D = \frac{d\theta'}{dE} = \frac{(b+1)\tan\theta}{E}, \tag{4.1}$$

where θ' is the reflected angle at the working energy E, and

$$b = -\frac{\sin(\theta_B + \eta)}{\sin(\theta_B - \eta)} \tag{4.2}$$

is the asymmetry factor[29]. It can be shown that the energy resolution of the monochromator is given by

$$\Delta E_m = \frac{\Delta E_i}{|b|} \tag{4.3}$$

where

$$\Delta E_i = \frac{\Delta\theta_D \, E}{\tan\theta_B} \tag{4.4}$$
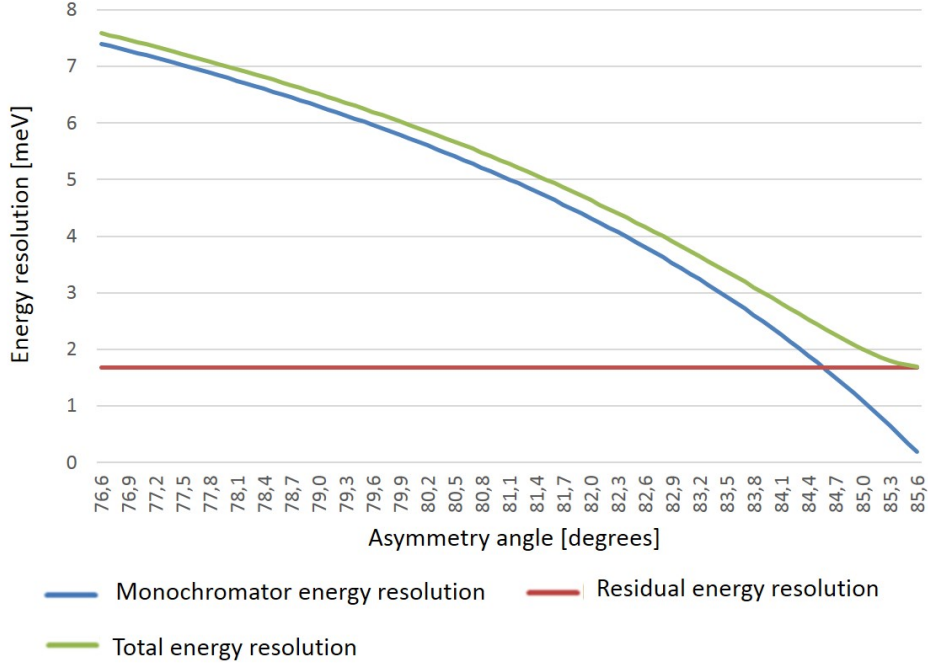
Figure 4.3: The energy resolutions with and without the residual component, as a function of the asymmetry angle η.

is the intrinsic energy resolution of the Si(884) reflection. From Equation (4.3), it turns out that the energy resolution can be made arbitrarily small by tuning the parameter b, as it can be seen in Figure 4.3. However, one should realise that the transmission of the monochromator scales like $1/|b|$, implying that the better the energy resolution the smaller the photon flux at the sample. We have chosen $|b|$ such that the flux reduction compared to the symmetric case is, say, $1/5$, i.e. we impose $|b| = 5$. This condition is met for $\eta = 83.6°$. The corresponding angular dispersion rate is $D = -5$ meV/μrad at $\theta_B = 85.70°$ ($E = 11215$ eV) and the calculated energy resolution is $\Delta E_m = 3$ meV. The finite residual beam divergence $\Delta\theta_r$ will contribute to the energy resolution with

$$\Delta E_r = \frac{\Delta\theta_r \ E}{\tan\theta_B}. \tag{4.5}$$

When a residual beam divergence of $\Delta\theta_r = 2$ μrad (we assume it to be completely dominated by the slope error $\delta_{SE} \approx 1$ μrad of the collimating mirror) is taken into account, the ultimate energy resolution does not change much.

The effect of the intrinsic angular divergence on the energy resolution is also shown in Figure 4.3 as a function of the asymmetry angle.

In addition to the flux reduction of about a factor 5 compared to the symmetric case, the asymmetrically-cut crystal degrades the focus of the beam at the sample position. This is due to the fact that it introduces a dispersion, which in turn can be interpreted as arising from a virtual source located at a finite distance. This is then imaged by the optical elements of the beam line, thus introducing an additional contribution to the focus at the sample position. Since the latter acts as the source size of the spectrometer, it can influence its performances. It is therefore crucial to estimate the effect of the CDW-like monochromator on the beam size at the sample position. This will be considered and investigated in the next section by means of ray-tracing simulations.

4.2 Parameter optimization with SHADOW

In the previous sections, we estimated the energy-resolution of the monochromator on the basis of analytical calculations. It is, however, possible to fine tune the parameters of the optical elements and have more reliable estimates of the energy-resolution by simulating the set-up with numerical codes. In addition, we want to estimate the beam size degradation at the sample position, as this affects the energy-resolution of the RIXS spectrometer. All the simulations regarding this new layout were performed using the SHADOW code.

4.2.1 What is SHADOW?

SHADOW is a ray-tracing program developed by F. Cerrina *et al.* at the University of Wisconsin. This program utilises a visual user interface (SHADOWVUI) developed by M. Sànchez del Rìo at the ESRF[27, 28]. SHADOW is especially optimized for the design of synchrotron radiation beam line optics, since it generates and traces a X-ray beam through an optical system. The *beam* is simulated by a collection of *rays* and the beam line by a collection of *optical elements*, e.g. mirrors, multilayers or crystals, placed in a sequential order.

The *source* is generated by choosing the spatial and angular distribution of X-rays, as well as their energy bandwidth, using a Monte Carlo method. For

η [degrees]	ΔE_{m1}^{calc} [meV]	ΔE_{m2}^{calc} [meV]	ΔE_{m1}^{sim} [meV]	ΔE_{m2}^{sim} [meV]
84.6	5.1	1.8	4.8	1.8
83.6	6.6	3.0	6.4	3.0
82.6	7.7	4.0	7.4	4.0
81.6	8.5	4.9	8.1	4.5
80.6	9.1	6.1	9.7	5.0
0	14.7	14.7	14	13

Table 4.1: Comparison between calculated and simulated energy resolution downstream the first asymmetrically-cut and second symmetrically-cut Si(844) crystal as a function of the asymmetry angle, considering a point source and without divergence.

any optical element, the parameters can be input manually or calculated by SHADOW itself. SHADOW traces the X-rays sequentially through each individual optical element[30]. It is then possible to visualise the spatial and angular distribution, as well as the energy and the intensity of the beam. In this way, one can study the effect of the beam line configuration and/or single optical element parameters on the characteristics of the beam. We focus here on the energy resolution and spatial distribution of the beam at the sample position as a function of the asymmetry angle of the crystal monochromator.

4.2.2   Simulations and numerical results

In order to better understand the complex optical set-up, simulations were initially performed by considering an ideal source, i.e. with no spatial and angular extensions. At a later stage, realistic parameters were introduced in order to properly characterize the beam line performances in terms of focal spot size at the secondary source and sample positions, as well as in terms of energy resolution.

The results of the first simulation with a point source are shown in Table 4.1, where both the energy resolution after the antisymmetric and symmetric crystals are reported and compared to the calculated ones. As it can be seen, a study of the variation of the energy resolution with the asymmetry angle is reported, considering not only the "rainbow" monochromator case ($\eta = 83.6°$) but also the symmetric ($\eta = 0°$) and some intermediate cases. The simulation results are comparable to the analytical calculations in some

Source parameters		
Spatial shape (V x H)	11.2 x 401.5 μm^2 rms	gaussian
Angular distribution (V x H)	5.6 x 11 μrad^2 rms	gaussian
Energy distribution	11215 eV $\pm$ 100 meV	uniform
Number of rays	100000	

Table 4.2: SHADOW source parameters.

cases, especially for $\eta = 83.6°$ they are identical. It is also clear that when η becomes bigger the energy resolution tends to zero. This would suggest to choose the crystal with the largest asymmetry angle, but this would lead to a tremendous loss of flux and to a broadening of the focus, which is minimum for the symmetric case and becomes larger while increasing the asymmetry angle. Indeed, the focus in the vertical direction, both for the SS1 and the sample position is very small for the symmetric case and significantly increases when introducing the asymmetrically-cut crystal.

While in the previous case neither the beam source size nor the beam divergence were considered, now these parameters are introduced to better simulate the synchrotron beam and to have more realistic results. The source parameters are shown in Table 4.2. In these simulations we also introduce the slope errors of the various optical elements as reported in Section 2.2. Simulations of the energy resolution and focus at both the secondary source and the sample position were performed as a function of the asymmetry angle and compared to the calculated energy resolutions in Table 4.3. It is not surprising that the energy resolution improves, while the spot size at both the secondary source and the sample position degrades with increasing asymmetry angle. In particular, Figure 4.4 shows that the simulated energy resolution is 3.4 meV for an asymmetry angle of 83.6°, in good agreement with the previous calculations, suggesting that we have a good understanding of the contributions to the energy resolution. For the same asymmetry angle, instead, we report in Figure 4.5 the simulated spot at the sample position to be about 16 x 10 μm^2 (V x H), to be compared to 6 x 10 μm^2 (V x H) in the symmetric case. These results finally seem to be comparable to the analytical calculations, proving that such monochromator can be implemented in the beam line to obtain an energy resolution which is considerably better than today.
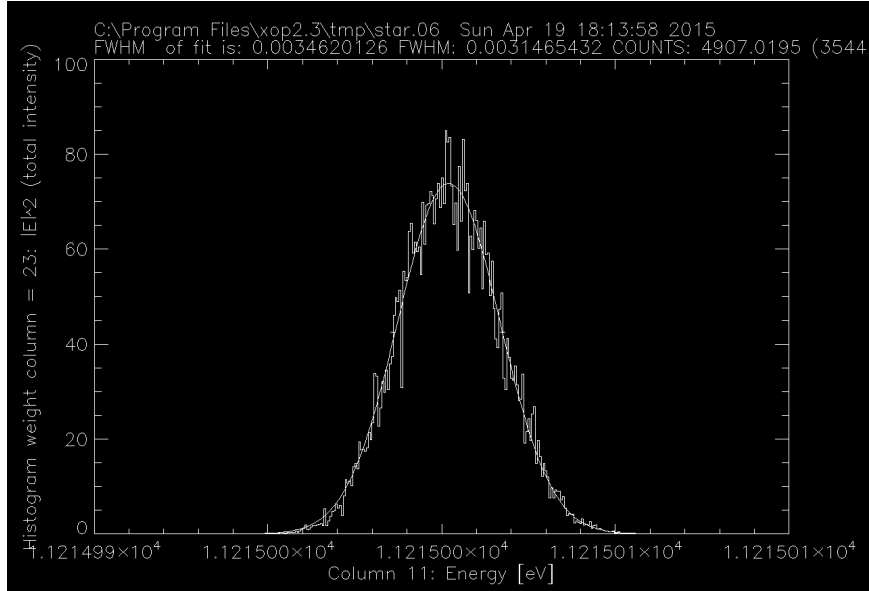
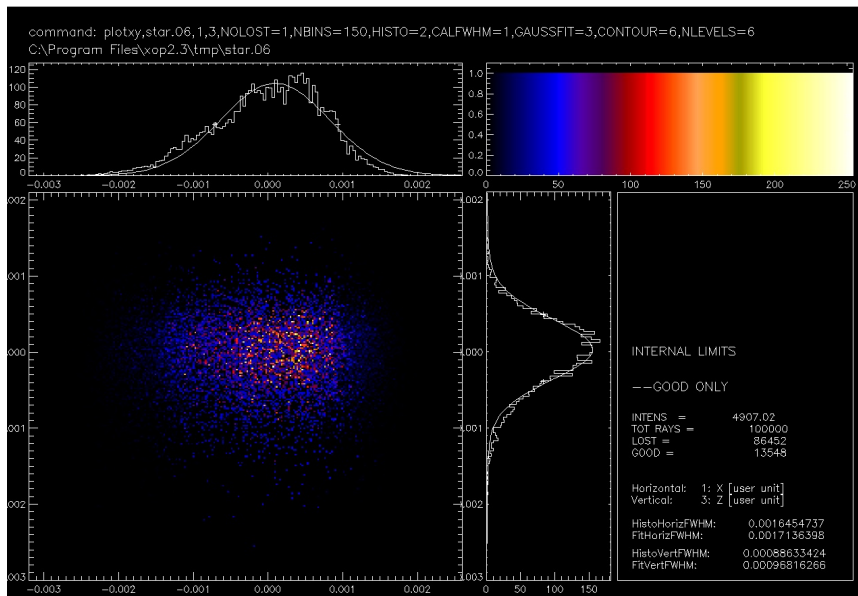**Figure 4.4:** Energy resolution after the symmetrical crystal.

Figure 4.5: The focus at sample position.

η [degrees]	ΔE_{mc} [meV]	ΔE_{ms} [meV]	Focus at SS1 [μm^2]	Focus at sample [μm^2]
84.6	1.8	2.7	220 x 220	19 x 10
83.6	3.0	3.4	160 x 220	16 x 10
82.6	4.0	4.2	150 x 220	15 x 10
81.6	4.9	4.8	140 x 220	14 x 10
80.6	6.1	5.4	130 x 220	13 x 10
0	14.7	13	50 x 220	6 x 10

Table 4.3: Calculated and simulated energy resolution, and simulated beam size at SS1 and the sample position (V x H) as a function of the asymmetry angle, considering slope errors and source parameters.
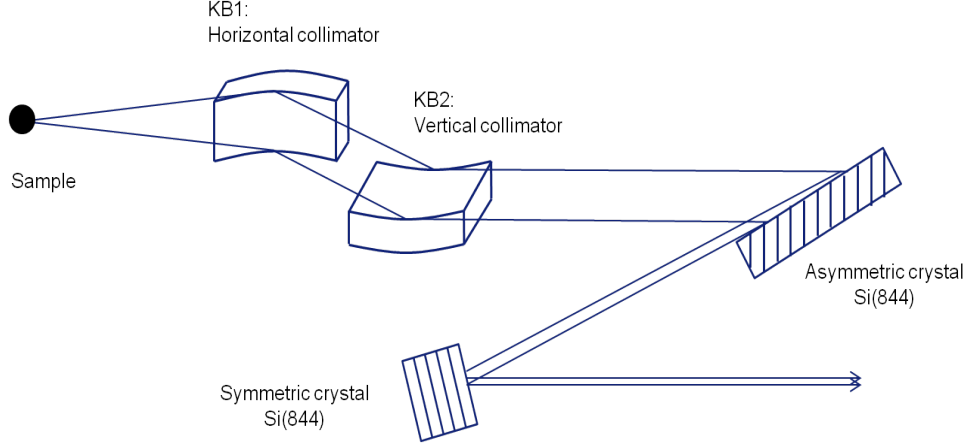
4.3 Spectrometer

As in the case of the "rainbow" monochromator, the spectrometer could be based on the CDW layout. However, the additional complication here is that the X-rays diffused by the sample must be collimated before they impinge on the asymmetrically-cut crystal. For this reason, we propose to use a KB mirror system, based on diffracting multilayers in order to increase the collected solid angle. The spectrometer optical layout is shown in Figure 4.6. The first mirror collimates the radiation in the horizontal direction, while the second mirror, rotated by 90° with respect to the first one, collimates the radiation in the vertical direction. We tentatively set their length to 300 mm, and the angle of incidence to $\theta_0 = 1.58°$ with respect to the surface, which corresponds to a multilayer periodicity of 2 nm. We set the distances between the sample and the centre of the mirrors at $f_1 = 400$ mm and $f_2 = 1600$ mm, respectively. Therefore, the solid angle which is intercepted is $\alpha = L \sin \theta_0 / f$, which corresponds to $\alpha_V \times \alpha_H = 5 \times 20$ mrad^2.

Given the distance from the source and the working angle, the radius of curvature of the mirrors can be calculated according to

$$R = \frac{2f}{\sin \theta_0}, \qquad (4.6)$$

where the image point has been set to infinity. We obtain $R_1 = 30$ m for the first mirror and $R_2 = 116$ m for the second mirror.

In the ideal scenario of a perfectly collimated beam, the energy resolution of this set-up would be identical to the one calculated above for the monochro-

Figure 4.6: Optical lay-out of the spectrometer.

Asymmetry angle	Focus at sample position (V x H)	Spectrometer resolution	Total resolution
[degrees]	[μm^2]	[meV]	[meV]
84.6	19 x 10	9.8	9.9
83.6	16 x 10	10.0	10.4
82.6	15 x 10	10.3	11
81.6	14 x 10	10.7	11.6
80.6	13 x 10	11	12.2

Table 4.4: Variations of spectrometer and total energy resolution as a function of the asymmetry angle.

mator, i.e. $\Delta E_m \sim 3$ meV for $\eta = 83.6°$. However, the finite size of the source and the mirror slope errors contribute to the residual divergence of the beam $\Delta\theta_r$, which ultimately degrades the energy resolution of the spectrometer. The source size contribution is given by $\Delta\theta_s = s/f_2$, where s is the size of the source. Note that the horizontal source size contributes marginally and therefore will be neglected. The second contribution to the residual divergence of the beam is the slope error δ_{se} of the vertically collimating mirror (we again neglect the slope error of the horizontally collimating mirror because, as it was the case for the horizontal source size, this contributes marginally to the residual divergence). In this case, we have $\Delta\theta_{se} = 2\delta_{se} \sim 2$ μrad. The combination of the two effects produce a residual divergence of the beam of $\Delta\theta_r = \sqrt{\Delta\theta_s^2 + \Delta\theta_{se}^2}$, which contributes to the energy resolution by about 9.5 meV at all asymmetry angles, accord-

ing to Equation 4.5. Considering the intrinsic energy resolution of the DW set-up, we obtain $\Delta E_s = \sqrt{\Delta E_r^2 + \Delta E_m^2}$ for the energy resolution of the spectrometer. This value of energy resolution has now to be convoluted with the one of the monochromator:

$$\Delta E_{\text{tot}} = \sqrt{\Delta E_{\text{m}}^2 + \Delta E_{\text{s}}^2}. \tag{4.7}$$

The results for different asymmetry angles, and thus different foci at the sample position, are summarized in Table 4.4. Under ideal conditions of zero slope error and source size, this set-up would give a very high energy resolution, but the residual divergence due to the finite source size and mirror slope error limits to a large extent the achievable energy resolution to a moderate value. Possible solutions are to increase the distance between sample and second mirror or to use a mask to reduce the finite source size contribution. In the first case the solid angle would be compromised and in the second case the beam flux would decrease dramatically.

4.4 Further improvements

Another possible method to improve the energy resolution is to select a different material for the spherical analyser crystals. So far, the availability of high quality crystals limited the use of material different than Si, but nowadays sufficiently large (almost) perfect crystals of Ge, SiO_2 (quartz), Al_2O_3 (sapphire), $LiNbO_3$ are also available for the production of analysers. For the specific case of Ir L_3 edge RIXS, the α-SiO_2(039) reflection can be used. This material has a Darwin width of 6 μrad and gives an intrinsic energy resolution of $\Delta E_i = 2$ meV. The contribution of the finite source-size is $\Delta E_s = 2.4$ meV, considering a typical source size of 15 μm. The pixel size gives a contribution of $\Delta E_p = 4.4$ meV. With these parameters the spectrometer energy resolution is 5.4 meV. To calculate the total energy resolution also the Si(844) post-monochromator must be taken into account and, in the case of η=83.6, one obtains a final resolution of 6 meV, as shown in Figure 4.7.

Even if the energy resolution is very high, this solution is not simple to implement and α-SiO_2(039) analysers are still at an early stage of development. In fact, recover and cut diced analysers of α-SiO_2(039) is not trivial; more-
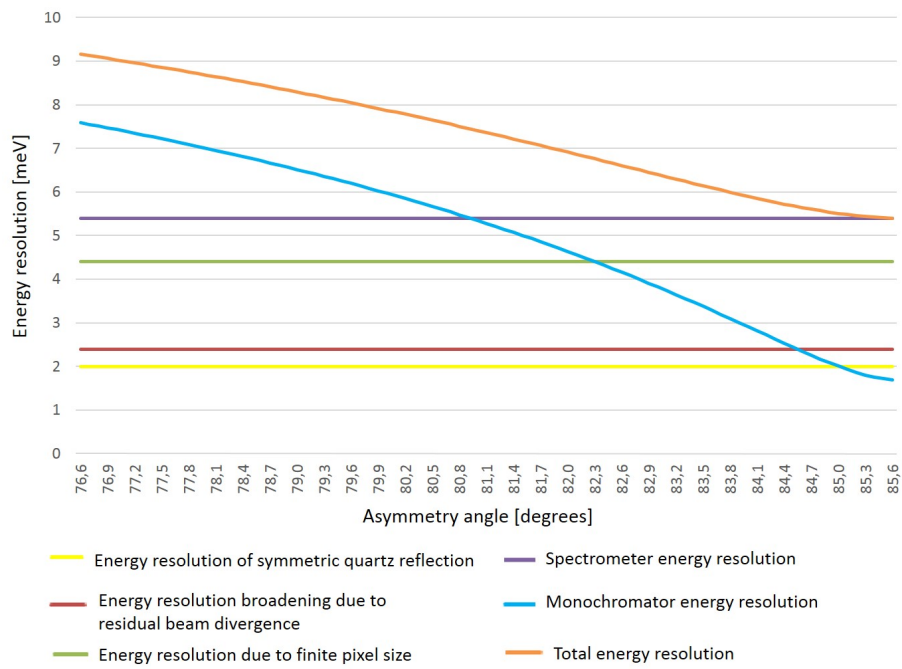
Figure 4.7: Contributions to the total energy resolution for a spectrometer with α-SiO$_2$(039) analysers.

over, the costs would be elevated. For this reason we are still in the process of evaluating the best solution to adopt for implementation on ID20.

Chapter 5

Conclusions

The present thesis deals with the study of magnetic excitations in $Sr_3Ir_2O_7$ under high pressure and the conceptual design of a new optical layout which will allow us to reach energy resolutions as good as 5 meV in Ir L_3 edge RIXS experiments.

$5d$ transition metal oxides have recently attracted much attention due to their unexpected insulating behaviour. However, while the transport properties have been satisfactorily explained by considering the effect of a large spin-orbit coupling on the Ir $5d$ states (giving rise to the so-called $J_{\text{eff}} = 1/2$ model), a clear description of the magnetic excitation spectrum of $Sr_3Ir_2O_7$ is still missing. In particular, at least two theories were proposed to explain the observed dispersion curves, but none of them seems to be able to explain all the experimental findings. RIXS measurements shown in this work aimed at studying magnetic excitations under high pressure, thus enlarging the experimental basis to test current or future theories. We were able to collect the energy-loss spectra at four reciprocal lattice points at three different pressures (1, 3 and 6 GPa). Our main result is that the acoustic and the optical modes have opposite behaviours: while the optical mode moves to lower energies as the pressure increases, the acoustic one moves to higher energies. In any case, we here would like to emphasize that our results are the first RIXS measurements of magnetic excitations at high pressure. Although we believe that additional data at even higher pressure would be beneficial to solve the puzzle of magnetic excitations in $Sr_3Ir_2O_7$, we believe that our experiment will pave the way for future high pressure RIXS studies of magnetic excitations.

Based on the observation that the acoustic and the optical branches in $Sr_3Ir_2O_7$ cannot be resolved individually because they are almost degenerate (within ~ 5 meV) and that their width is limited by the instrumental energy resolution, we performed a study on the possibility to improve the energy resolution of the set-up down to, say, ~ 5 meV. This implies that both the beam line monochromator and spectrometer should be changed accordingly. We propose for the former an asymmetrically-cut crystal, which causes the beam to be dispersed in a fan like in a prism, in combination with a symmetrically-cut crystal, which selects a specific wavelength. The energy resolution obtained for the monochromator is 3.4 meV for an angle of asymmetry of 83.6°. The spectrometer could be based on the same "rainbow" concept, with a KB mirror system to collimate the beam scattered by the sample. It turns out, however, that the residual divergence of the beam mostly due to the finite source size of the focus at the sample position compromises the ultimate energy resolution. For this reason, we alternatively propose a RIXS spectrometer similar to the one presently used at beam line ID20, but with a-SiO2(039) analysers, for which an energy resolution of 5 meV could be achieved. Because of the difficulty of implementation of these new analysers, however, we are still evaluating the best solution for ID20.

Bibliography

[1] Luuk J. P. Ament, Michel van Veenendaal, Thomas P. Devereaux, John P. Hill, and Jeroen van den Brink. Resonant inelastic X-ray scattering studies of elementary excitations. *Rev. Mod. Phys.*, 83: 705–767, Jun 2011. doi: 10.1103/RevModPhys.83.705. URL http://link.aps.org/doi/10.1103/RevModPhys.83.705.

[2] Xuan Gao. *Development of Polarization Analysis of Resonant Inelastic X-Ray Scattering.* PhD thesis, Western Michigan University ScholarWorks at WMU.

[3] Trinanjan Datta. *Resonant Inelastic X-ray Scattering.* The Net Advance of Physics: SPECIAL REPORTS, First Edition, 2002 June 11.

[4] J. P. Hill, G. Blumberg, Young-June Kim, D. S. Ellis, S. Wakimoto, R. J. Birgeneau, Seiki Komiya, Yoichi Ando, B. Liang, R. L. Greene, D. Casa, and T. Gog. Observation of a 500 meV collective mode in $La_{2-x}Sr_xCuO_4$ and Nd_2CuO_4 using resonant inelastic X-ray scattering. *Phys. Rev. Lett.*, 100:097001, Mar 2008. doi: 10.1103/PhysRevLett.100.097001. URL http://link.aps.org/doi/10.1103/PhysRevLett.100.097001.

[5] L. Braicovich, J. van den Brink, V. Bisogni, M. Moretti Sala, L. J. P. Ament, N. B. Brookes, G. M. De Luca, M. Salluzzo, T. Schmitt, V. N. Strocov, and G. Ghiringhelli. Magnetic excitations and phase separation in the underdoped $La_{2-x}Sr_xCuO_4$ superconductor measured by resonant inelastic X-ray scattering. *Phys. Rev. Lett.*, 104:077002, Feb 2010. doi: 10.1103/PhysRevLett.104.077002. URL http://link.aps.org/doi/10.1103/PhysRevLett.104.077002.

[6] Jungho Kim, D. Casa, M. H. Upton, T. Gog, Young-June Kim, J. F. Mitchell, M. van Veenendaal, M. Daghofer, J. van den Brink,

G. Khaliullin, and B. J. Kim. Magnetic excitation spectra of Sr_2IrO_4 probed by resonant inelastic X-ray scattering: establishing links to cuprate superconductors. *Phys. Rev. Lett.*, 108:177003, Apr 2012. doi: 10.1103/PhysRevLett.108.177003. URL http://link.aps.org/doi/10.1103/PhysRevLett.108.177003.

[7] ESRF. What is a synchrotron?

[8] N. Ashcroft and N. Mermin. *Solid state physics*. Science: Physics (Saunders College, 1976).

[9] AQR Barona, Yoshikazu Tanakab, D. Miwab, D. Ishikawab, T. Mochizukia, H. Kimurac, F. Yamamotoc, and T. Ishikawaab. Recent advances in instrumentation for high resolution inelastic X-ray scattering and nuclear resonant scattering.

[10] H. Sinn, E. E. Alp, A. Alatas, J. Barraza, G. Bortel, E Burkel, D Shu, W Sturhahn, J. P. Sutter, T. S. Toellner, et. al. An inelastic X-ray spectrometer with 2.2 meV energy resolution. *Nuclear Instruments and Methods in Physics Research Section A: Accelerators, Spectrometers, Detectors and Associated Equipment*, 467:1545–1548, 2001.

[11] C. Masciovecchio, U. Bergmann, M. Krisch, G. Ruocco, F. Sette, and R. Verbeni. A perfect crystal X-ray analyser with 1.5 meV energy resolution. *Nuclear Instruments and Methods in Physics Research Section B: Beam Interactions with Materials and Atoms*, 117(3):339 – 340, 1996. ISSN 0168-583X. doi: http://dx.doi.org/10.1016/0168-583X(96)00334-5. URL http://www.sciencedirect.com/science/article/pii/0168583X96003345.

[12] M. Moretti Sala, C. Henriquet, L. Simonelli, R. Verbeni, and G. Monaco. High energy-resolution set-up for ir L_3 edge RIXS experiments. *Journal of Electron Spectroscopy and Related Phenomena*, 188(0):150 – 154, 2013. ISSN 0368-2048. doi: http://dx.doi.org/10.1016/j.elspec.2012.08.002. URL http://www.sciencedirect.com/science/article/pii/S0368204812001077. Progress in Resonant Inelastic X-Ray Scattering.

[13] S. Huotari, Gy. Vankó, F. Albergamo, C. Ponchut, H. Graafsma, C. Henriquet, R. Verbeni, and G. Monaco. Improving the performance

of high-resolution X-ray spectrometers with position-sensitive pixel detectors. *Journal of Synchrotron Radiation*, 12(4):467–472, Jul 2005. doi: 10.1107/S0909049505010630. URL http://dx.doi.org/10.1107/S0909049505010630.

[14] G. Cao, J. Bolivar, S. McCall, J. E. Crow, and R. P. Guertin. Weak ferromagnetism, metal-to-nonmetal transition, and negative differential resistivity in single-crystal Sr_2IrO_4. *Phys. Rev. B*, 57:R11039–R11042, May 1998. doi: 10.1103/PhysRevB.57.R11039. URL http://link.aps.org/doi/10.1103/PhysRevB.57.R11039.

[15] G. Cao, Y. Xin, C. S. Alexander, J. E. Crow, P. Schlottmann, M. K. Crawford, R. L. Harlow, and W. Marshall. Anomalous magnetic and transport behavior in the magnetic insulator $Sr_3Ir_2O_7$. *Phys. Rev. B*, 66:214412, Dec 2002. doi: 10.1103/PhysRevB.66.214412. URL http://link.aps.org/doi/10.1103/PhysRevB.66.214412.

[16] B. J. Kim, Hosub Jin, S. J. Moon, J.-Y. Kim, B.-G. Park, C. S. Leem, Jaejun Yu, T. W. Noh, C. Kim, S.-J. Oh, J.-H. Park, V. Durairaj, G. Cao, and E. Rotenberg. Novel $J_{\text{eff}} = 1/2$ mott state induced by relativistic spin-orbit coupling in Sr_2IrO_4. *Phys. Rev. Lett.*, 101:076402, Aug 2008. doi: 10.1103/PhysRevLett.101.076402. URL http://link.aps.org/doi/10.1103/PhysRevLett.101.076402.

[17] B. M. Wojek, M. H. Berntsen, S. Boseggia, A. T. Boothroyd, D Prabhakaran, D F McMorrow, H. M. Rønnow, J. Chang, and O. Tjernberg. The $J_{\text{eff}} = \frac{1}{2}$ insulator $Sr_3Ir_2O_7$ studied by means of angle-resolved photoemission spectroscopy. *Journal of Physics: Condensed Matter*, 24(41): 415602, 2012. URL http://stacks.iop.org/0953-8984/24/i=41/a=415602.

[18] M. Moretti Sala, S. Boseggia, F. McMorrow, D. and G. Monaco. Resonant X-ray scattering and the J_{eff}=1/2 electronic ground state in iridate perovskites. *Phys. Rev. Lett.*, 112:026403, Jan 2014. doi: 10.1103/PhysRevLett.112.026403. URL http://link.aps.org/doi/10.1103/PhysRevLett.112.026403.

[19] D. A. Zocco, J. J. Hamlin, B. D. White, B. J. Kim, J. R. Jeffries, S. T. Weir, Y. K. Vohra, J. W. Allen, and M. B. Maple. Persis-

tent non-metallic behavior in Sr_2IrO_4 and $Sr_3Ir_2O_7$ at high pressures. *Journal of Physics: Condensed Matter*, 26(25):255603, 2014. URL http://stacks.iop.org/0953-8984/26/i=25/a=255603.

[20] M. A. Subramanian, M. K. Crawford, and R. L. Harlow. Single crystal structure determination of double layered strontium iridium oxide $Sr_3Ir_2O_7$. *Materials research bulletin*, 29(6):645–650, 1994.

[21] Hirofumi Matsuhata, Ichiro Nagai, Yoshiyuki Yoshida, Sigeo Hara, Shin-ichi Ikeda, and Naoki Shirakawa. Crystal structure of $Sr_3Ir_2O_7$ investigated by transmission electron microscopy. *Journal of Solid State Chemistry*, 177(10):3776–3783, 2004.

[22] S. Boseggia, R. Springell, H. C. Walker, A. T. Boothroyd, D. Prabhakaran, D. Wermeille, L. Bouchenoire, S. P. Collins, and D. F. McMorrow. Antiferromagnetic order and domains in $Sr_3Ir_2O_7$ probed by X-ray resonant scattering. *Phys. Rev. B*, 85:184432, May 2012. doi: 10.1103/PhysRevB.85.184432. URL http://link.aps.org/doi/10.1103/PhysRevB.85.184432.

[23] Jungho Kim, A. H. Said, D. Casa, M. H. Upton, T. Gog, M. Daghofer, G. Jackeli, J. van den Brink, G. Khaliullin, and B. J. Kim. Large spinwave energy gap in the bilayer iridate $Sr_3Ir_2O_7$: evidence for enhanced dipolar interactions near the Mott metal-insulator transition. *Phys. Rev. Lett.*, 109:157402, Oct 2012. doi: 10.1103/PhysRevLett.109.157402. URL http://link.aps.org/doi/10.1103/PhysRevLett.109.157402.

[24] D. Reznik, P. Bourges, H. F. Fong, L. P. Regnault, J. Bossy, C. Vettier, D. L. Milius, I. A. Aksay, and B. Keimer. Direct observation of optical magnons in $YBa_2Cu_3O_{6.2}$. *Phys. Rev. B*, 53:R14741–R14744, Jun 1996. doi: 10.1103/PhysRevB.53.R14741. URL http://link.aps.org/doi/10.1103/PhysRevB.53.R14741.

[25] arxiv:1506.04877 (2015) M. Moretti Sala et. al.

[26] H. Yavaş, M. van Veenendaal, J. van den Brink, L. J. P. Ament, A. Alatas, B. M. Leu, M. O. Apostu, N. Wizent, G. Behr, W. Sturhahn, H. Sinn, and E. E. Alp. Observation of phonons with resonant inelastic X-ray scattering. *Journal of Physics: Condensed Matter*, 22(48):485601, 2010. URL http://stacks.iop.org/0953-8984/22/i=48/a=485601.

[27] F. Cerrina and M. Sànchez del Rìo. *Ray Tracing of X-Ray Optical Systems.* Ch. 35 in Handbook of Optics (volume V, 3rd edition), edited by M. Bass, Mc Graw Hill, New York, 2009.

[28] Manuel Sanchez del Rio, Niccolo Canestrari, Fan Jiang, and Franco Cerrina. Shadow3 : a new version of the synchrotron X-ray optics modelling package. *Journal of Synchrotron Radiation*, 18(5):708–716, 2011. ISSN 0909-0495. doi: 10.1107/S0909049511026306.

[29] Yuri Shvyd'ko, Stanislav Stoupin, Kiran Mundboth, and Jungho Kim. Hard-X-ray spectrographs with resolution beyond 100 μeV. *Phys. Rev. A*, 87:043835, Apr 2013. doi: 10.1103/PhysRevA.87.043835. URL http://link.aps.org/doi/10.1103/PhysRevA.87.043835.

[30] M. Sànchez del Rìo. The very basic of shadow.

Acknowledgements

I am truly grateful to all the people I have met in these past years.

First of all I would like to thank Prof. Giacomo Ghiringhelli, who gave me the amazing opportunity to be a trainee at ESRF for eight months, and Dr. Michael Krisch for hosting me at beam line ID20 and for his competence and courtesy. I would like to thank particularly my supervisor Dr. Marco Moretti, for his guidance, his patience in always helping me and his friendliness. Thanks to Matteo Rossi, for his friendship and for being the best office mate ever, and to all the beam line ID20 staff: Christoph, Ali, Roberto and Christian.

Thanks to all the people I met in Grenoble for their friendship and support, I was very lucky to meet you: Silvia, Armelle, Andrea, Davide and all the others.

Thanks to all my Italian friends who helped me to soft my comeback, above all Benny, Laura, Giulia, Francesca, Elena and my cousin Beatrice.

Thanks to all my university mates who shared these past five years with me, in particular Smare, Marco rotA, Tommaso with Francesca and the little Elena, Mara, Fabio and all the others.

Finally I would particularly like to thank my parents, for always supporting me and for pushing me into doing always my best.

<div align="center">

My heartfelt gratitude to all of you,
Margherita Rezzaghi

</div>

<div align="center">

"Get a little rock and roll on the radio and go toward all the life there is with all the courage you can find and all the belief you can muster. Be true, be brave, stand. All the rest is darkness."
Stephen King, *It*

</div>